



# Strain localization by shear heating and the development of lithospheric shear zones



Katy Willis<sup>a,\*</sup>, Gregory A. Houseman<sup>b</sup>, Lynn Evans<sup>c</sup>, Tim Wright<sup>b</sup>, Andrew Hooper<sup>b</sup>

<sup>a</sup> School of Earth and Environment, University of Leeds, Leeds, UK

<sup>b</sup> COMET, School of Earth and Environment, University of Leeds, Leeds, UK

<sup>c</sup> Monash University, School of Earth, Atmosphere and Environment, Clayton, VIC 3800, Australia

## ARTICLE INFO

### Keywords:

Strain localization  
Strike-slip shear zone  
San Andreas Fault Zone  
North Anatolian Fault Zone  
Lithospheric deformation  
Continental tectonics

## ABSTRACT

Analogue and numerical models show that strong or weak domains in a deforming ductile material cause stress concentrations that may promote strain localization. Such domains commonly occur in the lithosphere through variations in composition or mineral fabric. Here we use a 2D plane-stress, non-Newtonian, viscous model to explore how strain localization develops from an initial isolated weak inclusion. We use a temperature-dependent rheological law for which the material weakens as a result of work done by shear converted to heat. The progress of strain localization follows a power-law growth that is strongly non-linear and may be regarded as an instability. Although this localization mechanism is ultimately limited by thermal diffusion, this parametrization permits a robust criterion for the conditions in which localized shear zones can form within the lithosphere. Shear zones in the lower crust are typically depicted as the downward continuation of faults. We argue that the depth-extent of narrow shear zones within the lithosphere is limited by the stability criteria that we infer from 2D numerical experiments. When applied to the rheological laws for common lithospheric minerals, the combination of temperature and stress-dependence provides a direct means of predicting the depth below which the localization instability does not occur. For an olivine based rheology, the maximum depth at which rapid localization is expected is in the range of ~20 to 60 km, depending on heat flow, strain-rate and water fugacity. We apply our calculations to two major continental strike-slip zones, the San Andreas Fault and North Anatolian Fault, and compare our predicted maximum localization depths with published seismological images. Strain localization in the lower crust requires a dry rheology comparable to plagioclase. Observations that imply localized strain in the uppermost mantle beneath these fault zones are consistent with the localization criteria and the rheological properties of dry olivine.

## 1. Introduction

Large scale deformation of the continents is reasonably well explained by simplified models in which the lithosphere behaves as a thin viscous sheet that responds to plate boundary stresses and internal variation of gravitational forces (e.g. England et al., 2016; England and Molnar, 2005). By averaging over the thickness of the lithosphere, such models can disregard the apparent localization of deformation associated with faults in the uppermost crust and localized shear zones that may be present at deeper levels. Although localized strain on major shear zones may play an important role in lithospheric-scale deformation (Thatcher and England, 1998; Kreemer et al., 2014), how ductile shear zones develop is poorly understood. Do they propagate from faults present in overlying layers (e.g. Moore and Parsons, 2015)? Or is surface fault expression a consequence of localization at depth from the

formation of ductile shear zones (e.g. Burgmann and Dresen, 2008)? Here we attempt to develop a simplified conceptual model in which we quantify how localization can develop in an initially homogeneous ductile medium due to shear heating. We then compare the predictions of this model with geophysical observations of strain localization from two major lithospheric shear zones.

Large-scale lateral variations in rheology of continental lithosphere arise through orogenesis, pluton emplacement, thermal evolution and other geological processes (Cloetingh et al., 2010). Molnar and Tapponnier (1981) pointed out that variations in age and thermal state apparently control the distribution of lithospheric-scale deformation in Central Asia. Analogue (Keep, 2000) and numerical (England and Houseman, 1985; Tommasi et al., 1995) models show how high- or low-viscosity domains within the deforming continental lithosphere can influence the strain distribution arising from plate boundary forces.

\* Corresponding author.

E-mail address: [eekeew@leeds.ac.uk](mailto:eekeew@leeds.ac.uk) (K. Willis).

<https://doi.org/10.1016/j.tecto.2019.05.010>

Received 12 December 2018; Received in revised form 7 May 2019; Accepted 9 May 2019

Available online 15 May 2019

0040-1951/ © 2019 Published by Elsevier B.V.

Strain typically localizes near domain boundaries between regions of different effective viscosity (Vauchez et al., 1998; Vauchez et al., 2012). Sustained deformation in this situation can create lithospheric-scale shear zones, such as the Altyn Tagh fault of Central Asia (Dayem et al., 2009) or the Borborema shear zone in Brazil (Tommasi and Vauchez, 1997; Tommasi et al., 1995). Under a convergent strain field, orogenic belts such as those bordering the Tarim Basin may develop (Calignano et al., 2015). Localization of deformation is enhanced when the resistance to deformation decreases with strain or strain-rate and Gueydan et al. (2014) argue that progressive strain localization is a precursor to the formation of tectonic plate boundaries.

Under convergent or divergent strain fields it is clear that weak layers within a vertically stratified lithosphere play an essential role in localizing deformation and allowing movement on faults and shear zones that sole into a ductile crustal layer (e.g., Beaumont et al., 2000). Analogue and numerical models of lithospheric deformation (e.g., Brun, 2002; Calignano et al., 2015; Munteanu et al., 2013; Sokoutis et al., 2005; Willingshofer et al., 2005) have provided essential insights into how a faulted upper crustal layer interacts with ductile deformation at depth. Although some studies have focussed on the process of strain localization in transpressional or transtensional environments (e.g., Cerca et al., 2004; Corti et al., 2002; Le Pourhiet et al., 2012) the simpler case of strike-slip deformation has attracted less attention, perhaps because orogenic belts and extensional basins are more commonly encountered. In this study we focus on how strain may localize in the strike-slip environment, and in particular address the question of the depth dependence of strain localization.

Strain distribution in viscous or visco-plastic flow models is generally controlled by the background stress field imposed at the boundaries of the domain, but the geometrical shape and alignment of anomalous inclusions can promote the formation of shear zones whether the inclusion is relatively weak (Mandal et al., 2004) or strong (Misra and Mandal, 2007). Shear zones originating from multiple anomalous domains can propagate and amalgamate under sustained strain (Grujic and Mancktelow, 1998; Mandal et al., 2004; Misra and Mandal, 2007). Analogue experiments by Misra et al. (2015) showed that increasing temperature inhibits localization as plastic strain is enabled across the deforming medium, while increasing pressure promotes localization.

Localization of strain may be enhanced by strain-rate weakening in regions where stress differences vary. For the non-Newtonian constitutive laws that typically describe creep deformation of silicates (Hirth and Kohlstedt, 1995; Karato, 1984; Karato et al., 1986; Kohlstedt and Goetze, 1974) effective viscosity is reduced where the concentration of intra-crystalline dislocations is increased in response to greater stress differences. However, the degree of localization evident in lithospheric-scale shear zones is not explained simply by power-law materials with typical stress versus strain-rate exponents of  $n \sim 3$  (Dayem et al., 2009). A strain-weakening process is also required to explain the formation of lithospheric shear zones like the Altyn Tagh, the San Andreas and the North Anatolian. Lithospheric-scale strain-weakening mechanisms based on fabric development (e.g. Montési, 2013) coupled to grain size sensitive creep (e.g. Precigout and Gueydan, 2009; Warren and Hirth, 2006) or shear heating (Brun and Cobbold, 1980; Burg and Schmalholz, 2008; Leloup et al., 1999; Regenauer-Lieb et al., 2015; Thielmann and Kaus, 2012) have been proposed. Independent of scale, localisation requires a weakening feedback mechanism that can depend on one or more variables, including changes in temperature and grain-size (Montési and Zuber, 2002). For any weakening mechanism, spatial variations in the work done by deformation cause variations in the strength of the material and thereby promote localization of deformation. Thielmann and Kaus (2012) showed that shear heating can facilitate the formation of a lithospheric-scale shear zone. Burg and Schmalholz (2008) showed how buckling of the lithosphere in a convergent environment gives way to localization of deformation on thrust planes. In some situations shear heating may

be sufficient to cause partial melting and extreme strain localization (Nicolas et al., 1977; Regenauer-Lieb et al., 2015). However, localization through shear-heating may be suppressed for temperatures greater than some threshold dependent on specific lithology (Montési and Zuber, 2002). We here focus on the thermal weakening model for strain localization, but comment that a similar approach could be used for modelling of possible localization mechanisms based on development of mineral fabric.

We use 2D numerical experiments to demonstrate how strain can localize around a weak seed in a lithospheric environment which would otherwise undergo homogeneous simple shear. We follow Grujic and Mancktelow (1998), Kaus and Podladchikov (2006) and Mandal et al. (2004) in examining how a weak seed influences strain distribution, but here consider a simple-shear deformation field, rather than pure-shear. Shear zone development might be triggered by any kind of stress concentration but, using a single weak seed, we estimate what is probably a lower bound on the rate of shear localization and avoid effects due to interacting shear zones (Grujic and Mancktelow, 1998; Mandal et al., 2004; Misra and Mandal, 2007). We use a simplified continuum model with a generalised strain-weakening rheological law based on temperature-activated dislocation creep in silicates to represent a thermal weakening mechanism. Conservation of energy implies that the work done by viscous strain causes a weakening dependent on the integrated work. When stress is relatively homogeneous, weakening is most effective in regions of greatest strain rate, thus promoting a feedback mechanism that leads to progressive strain localization. We quantify the rate of shear localization by focusing on the strain rate within a sheared region and show that it increases at a rate that is primarily determined by a dimensionless variable dependent on rheological parameters and environmental variables like temperature, pressure and background strain-rate. These experiments may be compared with similar experiments reported by Kaus and Podladchikov (2006) who obtained scaling laws for the rate of temperature increase and showed that the weakening mechanism may be suppressed by the effect of diffusive cooling.

Our 2D models may be seen as approximate representations of shear localization within a layer at constant depth in a strike-slip environment. By considering how temperature, pressure and mineralogy within the lithosphere affect the shear localization parameter, we then estimate whether thermally activated shear localization at any given depth in the lithosphere should be expected. With this mechanism, dominated by temperature, there is clearly a maximum depth at which shear can localize. While retaining a quantification of the problem based on the fundamental principle of conservation of energy, the approximations we use allow us to simplify the inherent complexity of the geological process, in order to determine some general rules and scaling laws that determine when we should expect strain localization to occur in the lithosphere in a strike-slip environment. We then compare maximum depths of shear localization inferred from seismic observations with the predictions of this simplified theory, for two major continental strike-slip systems.

## 2. A conceptual model of thermally activated strain weakening

A general creep law for silicates may be represented by:

$$\dot{\epsilon}_{ij} = A\theta^{n-1}\tau_{ij}f_{H_2O}^r s^{-m} \exp\left(\frac{-(Q+pV)}{RT}\right) \quad (1)$$

where  $\dot{\epsilon}_{ij}$  and  $\tau_{ij}$  are strain rate and deviatoric stress components respectively,  $\theta$  is the second invariant of the deviatoric stress, ( $\theta^2 = \tau_{ij}\tau_{ij}$ ),  $n$  is the power-law creep exponent,  $Q$  and  $V$  are the activation energy and volume respectively,  $T$  is the temperature in Kelvin,  $p$  is pressure,  $R$  is the universal gas constant,  $s$  is the grain size,  $f_{H_2O}$  is the fugacity of water,  $r$  and  $m$  are experimentally-determined indices, and  $A$  is an empirical constant determined by experiment. At low stress or high temperature, diffusion creep dominates,  $n$  is  $\sim 1$  and  $m > \sim 1$ . At

greater stress or lower temperature  $n > \sim 3$  and  $m$  is generally thought to be about zero, so that there is no grain-size sensitivity. In either case the effective viscosity is a strong function of temperature. In some studies  $V$  and  $r$  may be set to zero so that the pressure and fugacity dependences are omitted. Eq. (1) follows the notation of Hirth and Kohlstedt (2013) except that the stress dependence is represented using the frame invariant form  $\Theta^{n-1}\tau_{ij}$  rather than  $\sigma^n$  (axial stress in the experiments).

Shear heating arises from the conversion of mechanical work to heat. If the mechanical work is entirely dissipated, and deformation is rapid compared to thermal diffusion, the rate of temperature change ( $\partial T/\partial t$ ) is determined by conservation of energy:

$$\rho C_p \frac{\partial T}{\partial t} = \dot{\epsilon}_{ij} \tau_{ij} \quad (2)$$

for density  $\rho$  and heat capacity  $C_p$ .

The viscous deformation law described by Eq. (1) can be inverted and re-written using a strength coefficient  $B$  that includes the dependence on temperature, grain-size, fugacity, pressure, and the stress invariant  $\Theta$  is replaced by the strain-rate invariant  $\dot{E}$ :

$$\tau_{ij} = B \dot{E}^{(1-n)/n} \dot{\epsilon}_{ij} \quad \text{with } \dot{E} = \sqrt{\dot{\epsilon}_{ij} \dot{\epsilon}_{ij}} \quad (3)$$

In order to relate our non-dimensional numerical experiments to the physical context of the lithosphere, we firstly note that the inversion of Eq. (1) into Eq. (3) is achieved if

$$B = \left(\frac{2}{3}\right)^{(n+1)/2n} A^{-1/n} f_{H_2O}^{-r/n} \exp\left(\frac{Q+pV}{nRT}\right) s^{m/n} \quad (4)$$

We note here that in the experimental literature, rheological laws are usually reported for uniaxial compression in a form that is not frame-invariant (i.e., the stress dependence is written as the  $n^{\text{th}}$  power of the principal stress rather than in terms of the second invariant of deviatoric stress). Including the leading numerical factor in Eq. (4) takes account of this difference and allows us to use the coefficient  $A$  as reported by experimentalists, e.g. Hirth and Kohlstedt (2013).

The temperature-dependence defined in (4) allows us to calculate the rate at which this rheological factor changes as the temperature changes:

$$\frac{1}{B} \frac{dB}{dt} = \frac{-(Q+pV)}{nRT^2} \frac{dT}{dt} \quad (5)$$

If we assume that all the work dissipated by viscous deformation is converted into heat and locally retained on the time-scale of interest, then we follow Dayem et al. (2009) by substituting (2) and (3) into (5) to obtain:

$$\frac{1}{B} \frac{dB}{dt} = -\Gamma B \dot{E}^{(1+n)/n} \quad (6)$$

where

$$\Gamma = \left(\frac{Q+pV}{nRT^2}\right) \left(\frac{1}{\rho C_p}\right) \quad (7)$$

We also define a thermal anomaly parameter  $D$ , which represents the time-integrated work per unit volume and is proportional to the local increase in temperature if diffusion of heat is neglected:

$$D = \int_0^t B \dot{E}^{(1+n)/n} dt \quad (8)$$

so that (6) may be rewritten:

$$\frac{1}{B} \frac{dB}{dt} = -\Gamma \frac{dD}{dt} \quad (9)$$

Allowing that  $\Gamma$  is a function of  $T$  and hence  $B$ , we can integrate Eq. (9) to show (Appendix 1) that:

$$\ln\left(\frac{B_1}{B_0}\right) = -\sqrt{\Gamma_1 \Gamma_0} D \quad (10)$$

where  $B_0$  and  $\Gamma_0$  are the initial local strength coefficient and corresponding value of  $\Gamma$ , and  $B_1$  and  $\Gamma_1$  are the corresponding values after the deformation that produces the integrated work  $D(t)$ .

Using the initial temperature  $T_0$ , normalized by the other quantities in the Arrhenius term,

$$T_{ref} = \left(\frac{nRT_0}{Q+pV}\right) \quad (11)$$

we can manipulate Eq. (10) to give the local strength coefficient at any time  $t$ :

$$\ln B(t) = \frac{[\ln B_0 + (T_{ref} \ln B_0 - 1) \Gamma_0 D(t)]}{[1 + T_{ref} \Gamma_0 D(t)]} \quad (12)$$

Because local thermal anomalies can be attenuated by diffusion, we modify the numerical integration of Eq. (8) by including an additional term to represent approximately the effect of diffusion of heat away from a shear zone (refer Appendix 2):

$$\frac{dD}{dt} = B \dot{E}^{(1+n)/n} - \beta D \quad (13)$$

This correction factor approximates the decay of a thermal disturbance with a characteristic spatial wavenumber  $k$  in a uniform medium of diffusivity  $\kappa$  if  $D$  is proportional to the local thermal anomaly (Appendix 2) and

$$\beta = \kappa k^2 \quad (14)$$

This correction factor does not accurately deal with a more complex thermal disturbance, in which a range of wavelengths may be present and changing with time, but it allows us to examine qualitatively the effect of thermal diffusion in this problem for a range of plausible  $\beta$  values.

The rate of reduction of  $B$  varies spatially with the rate of strain, enabling lateral variations in  $B$  to develop across the viscous domain. Any heterogeneity in the strain-rate field, caused for example by irregular geometry or natural variation of the viscosity coefficient, can lead to increased rates of weakening in the places where strain-rates are greatest. If localized weakening in one place results in strain-rates decreasing elsewhere, then the viscosity coefficient will recover in the latter regions at a rate determined by  $\beta$ . Although this approximate formulation of strain weakening in the lithosphere has ignored numerous complexities that link deformation, micro-structure and thermal evolution, it enables a compact parameterization of the problem determined by simple physical principles of local heating and recovery, and controlled by the three parameters  $\Gamma_0$ ,  $\beta$  and  $T_{ref}$ , which may be thought of as determining the rate of weakening, the rate of recovery and the scaled background temperature.

In the following section we use numerical experiments to investigate how localization develops when triggered by a circular weak seed in a 2D plane-stress calculation driven by external shear. In these calculations the 2D plane is assumed horizontal so that the background temperature is uniform and the strain-rate field is representative of a strike-slip environment. The model geometry is ad hoc, but it enables us to identify some characteristics of localization in non-Newtonian thermally activated materials that are generally valid. Varying the shape of the weak seed would require adjustment to rates of localization, but the development of the localization is expected to follow a similar path.

In these numerical experiments we non-dimensionalize the physical variables as follows:

$$\dot{\epsilon} = \dot{\epsilon}_0 \dot{\epsilon}'; \quad B = H_0 B'; \quad \tau = H_0 \dot{\epsilon}_0^{1/n} \tau'; \quad D = H_0 \dot{\epsilon}_0^{1/n} D' \quad (15)$$

where  $\dot{\epsilon}_0$  is the background strain-rate, and  $H_0$  is a physical scale factor for the viscosity coefficient:

$$H_0 = \left(\frac{2}{3}\right)^{(n+1)/2n} [Af_{H_2O}^r s^{-m}]^{-1/n} \exp\left(\frac{Q + p_0 V}{nRT_0}\right) \quad (16)$$

and where  $T_0$  and  $p_0$  are the reference temperature and pressure at the depth that corresponds to the plane of the calculation. Hence, for consistency with Eqs. (7) and (9), the dimensionless localization parameter is:

$$\Gamma_0' = \Gamma_0 H_0 \dot{\epsilon}_0^{1/n} = \left(\frac{2}{3}\right)^{(n+1)/2n} \left(\frac{Q + p_0 V}{\rho C_p nRT_0^2}\right) [A^{-1} s^m f_{H_2O}^{-r} \dot{\epsilon}_0]^{1/n} \exp\left(\frac{Q + p_0 V}{nRT_0}\right) \quad (17)$$

The diffusion parameter  $\beta$  is rendered dimensionless after division by  $\dot{\epsilon}_0$ .

In Section 3 we use dimensionless values of  $\Gamma_0'$  to define the experimental problem. In Section 4 we consider how  $\Gamma_0'$  may vary with depth within the lithosphere using parameter values from experimental rheology in Eq. (17). In Section 5, we compare inferences from the numerical experiments using relevant strain-rate and geothermal parameter estimates with observations from actual lithospheric shear zones.

### 3. 2D numerical experiments on localization

As an initial exploration of the general strain localization problem in two dimensions we now consider a series of numerical experiments on a simplified model of 2D plane-stress deformation of a rectangular region undergoing simple shear imposed by boundaries moving at a constant rate (Fig. 1). We assume a non-linear viscous material with constitutive law defined by Eq. (3) and allow the rheological coefficient to evolve with time as defined by Eqs. (12)–(13). We use the finite element program *basil*, as previously used by Dayem et al. (2009), to obtain time-dependent solutions of the evolving deformation field by solving for the strain-rate field that satisfies the conditions of stress equilibrium and mass conservation, here amended to allow for temperature-dependent weakening factor  $\Gamma$  and diffusion factor  $\beta$ . For the following calculations, in which all parameters are dimensionless, we use a rectangular region of length 80 and width 8, with x-direction velocities of  $\pm 8$  imposed on the y-boundaries (Fig. 1) so that the background shear strain-rate is  $\dot{\epsilon}_0' = 1$ . The rheological coefficient  $B_0'$  is initially 1 everywhere. Using parameters for olivine (Hirth and Kohlstedt, 2013) and quartz (Hirth et al., 2001; Rutter and Brodie, 2004) and assuming  $V = 0$  (Table 1), dimensional values of  $\Gamma$  (Eq. (7)) vary between about  $6 \times 10^{-9}$  and  $3 \times 10^{-8} \text{ m}^3/\text{J}$  for temperatures between about 400 and 1000 K. Because the temperature dependence of the non-dimensionalizing factor (Eq. (17)) is so strong, the dimensionless  $\Gamma'$  value may vary over orders of magnitude within the lithosphere, though typically in the range 0.01 to 100. We find, however, that the range of interesting behaviour is much more restrictive, and our experiments focus on values of  $\Gamma_0'$  between 0.4 and 2.0. For the same parameters  $T_{ref}$  is typically in the range 0.03 to 0.1 but may be  $> 0.2$  for wet quartz. We use values of 0.041 and 0.148 representative of dry olivine at 1000 K and wet quartz at 600 K respectively in these experiments (Table 1). A representative

value of dimensionless  $\beta$  is between about 0.4 and 4 for a disturbance on a 10 km length scale and strain-rate between  $10^{-12}$  and  $10^{-13} \text{ s}^{-1}$  and it increases as the square of the wavenumber of the thermal disturbance.

As an initial test of the implementation of Eq. (12) in the finite deformation program *basil*, we set  $n = 3$ ,  $\Gamma_0' = 1$ ,  $\beta = 0$ , and  $T_{ref} = 0$ , 0.041 and 0.148 in order to test that the strain weakening works as expected for an initially homogeneous region under simple-shear boundary conditions, for which the rate of weakening is spatially invariant. The *basil* calculation closely tracks the theoretical relationship (Eq. (12)) between  $B'$  and  $D'$  as the strength of the material is reduced by a factor of about 5 in the three tests shown in Fig. 2. When  $T_{ref} = 0$ ,  $\Gamma$  is constant during the time integration and the theoretical model predicts exponential decay (a straight line on Fig. 2). We can see that, for these values of  $T_{ref}$ , assuming  $\Gamma$  is constant produces slightly faster localization, though the difference is small relative to the case with  $T_{ref} = 0.041$ .

To initiate strain localization we require some initial spatial heterogeneity. In reality any spatial heterogeneity can act as a seed for localization, but we attempt here to describe systematic behaviour in a particularly simple case: we embed a small circular inclusion (radius = 1) in the centre of our test region (Fig. 1). Within this circular patch the initial rheological factor  $B = \Lambda B_0$  is set. When a weak inclusion is present ( $\Lambda < 1$ ) and strain weakening is activated ( $\Gamma_0'$  sufficiently large) localized regions of high shear strain rate (relative to the background value) appear either side of the weak inclusion. These high strain-rate zones extend parallel to the shear direction and diminish in intensity with distance from the inclusion (Fig. 3). This strain-rate pattern contrasts with shear zones developed under pure shear, in which typically four high strain regions, aligned at between  $35^\circ$  and  $53^\circ$  to the principal axis develop away from an inclusion (Grujic and Mancktelow, 1998; Kaus and Podladchikov, 2006; Mandal et al., 2004). Depending on the strain-weakening parameters  $\Gamma_0'$  and  $T_{ref}$ , increasing boundary displacement causes the gradient of  $U_x$  within these zones to increase as that outside decreases, so that the total velocity contrast across the layer remains consistent with the boundary conditions (Fig. 4). We quantify strain localization by measuring the gradient  $dU_x/dy$  across the high strain-rate zone. Using this measure we track the development of the shear zone in time and distance from the weak inclusion (Fig. 5a, b).

For  $\beta = 0$  (no thermal diffusion) we see from the log-linear graph of Fig. 5c that the shear zone gradient has a growth curve that is faster than exponential, though the early phases of that growth may be approximated as exponential. We therefore investigated whether a power law growth of the form:

$$\left(\frac{dU_x}{dy}\right)_{sz} = a(t_0 - t)^{-p} \quad (18)$$

might describe the latter stage of these growth curves. To do so we plot, as a function of time, measured values of the shear-zone gradient raised to the power  $-1/p$  (as in Fig. 5d) for a range of  $p$ -values. In general the resulting graph is a straight line for some  $p$ -value after an initial phase

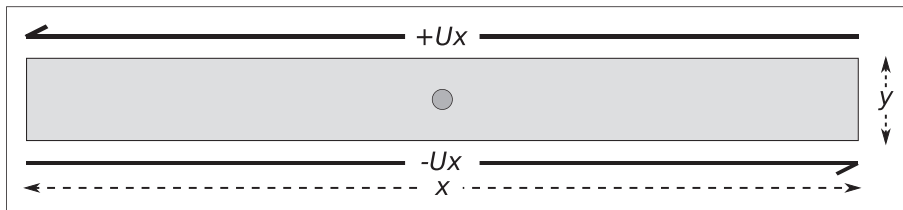
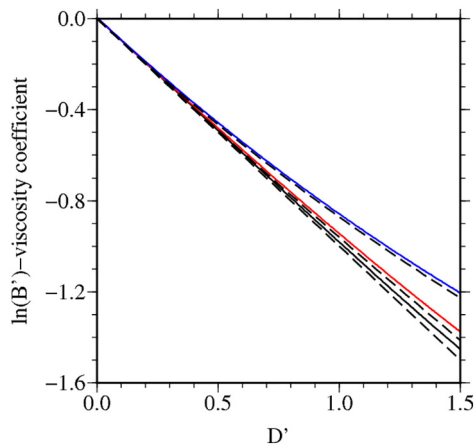


Fig. 1. The model domain is a rectangular region of length  $80r$  and width  $8r$  in the  $(x, y)$  plane with a circular inclusion of radius  $r = 1$  located centrally. The external boundary conditions ideally should be far enough from the inclusion that they do not affect the inhomogeneous part of the strain field in the locality of the inclusion. A velocity,  $U_x = \pm 8$  is applied to the horizontal boundaries such that the background strain rate = 1. The viscosity coefficient  $B'$  of the background region is initially set at  $B_0' = 1$  and the viscosity coefficient of the inclusion is initially weaker than the background region by a factor  $\Lambda$ .

**Table 1**  
Rheological parameters used in the calculation of the localization constant. Representative values of  $T_{ref}$  are given for two different temperatures.

Mineral	A	Q (kJ/mol)	n	V (m <sup>3</sup> /mol)	Deformation	Reference	$T_{ref}$	
							400 K	600 K
Quartz	1E-2.45	242	2.97	–	Dry dislocation	Rutter and Brodie (2004)	0.041	0.061
	1E-11.2	135	4	–	Wet dislocation (fugacity exponent = 1.0)	Hirth et al. (2001)	0.099	0.148
Plagioclase (An100)	5.01E12	648	3	–	Dry dislocation	Rybacki and Dresen (2000)		
	3.98E02	356	3	–	Wet dislocation		750 K	1000 K
Olivine	1.1E05	530	3.5	14	Dry dislocation	Hirth and Kohlstedt (2013)	0.041	0.055
	1600	520	3.5	22	Wet dislocation, (fugacity exponent = 1.2)		0.042	0.056



**Fig. 2.** Evolution of the strength coefficient  $B'$  and integrated work  $D'$  for an initially homogeneous region with  $n = 3$  and  $\Gamma_0' = 1.2$ . Solid lines show evolution calculated by finite element program *basil* where  $T_{ref} = 0$  (black), 0.041 (red) and 0.148 (blue). The black dashed lines show evolution calculated from Eq. (12) for corresponding  $T_{ref}$  values. (For interpretation of the references to colour in this figure legend, the reader is referred to the web version of this article.)

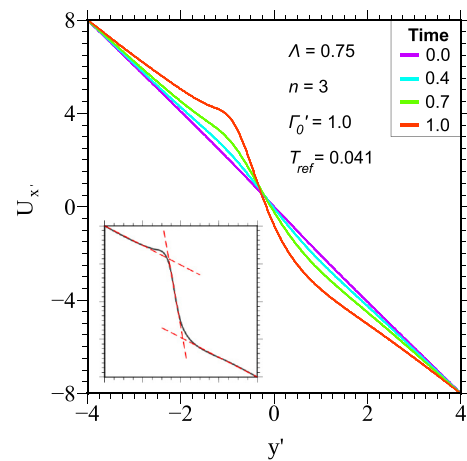


**Fig. 4.** Profiles of  $U_x$  across the strain-rate field shown in Fig. 3 at  $x = 4$  and times as labelled. At  $t = 0$  the  $dU_x/dy$  gradient is constant across the line of section. With increasing time (or strain) the gradient in the middle of the region,  $(dU_x/dy)_{sz}$ , increases but the total velocity difference across the region remains unchanged as strain-rates decrease outside the shear zone. The high gradient region corresponds to the developing high strain-rate zones as shown in Fig. 3.

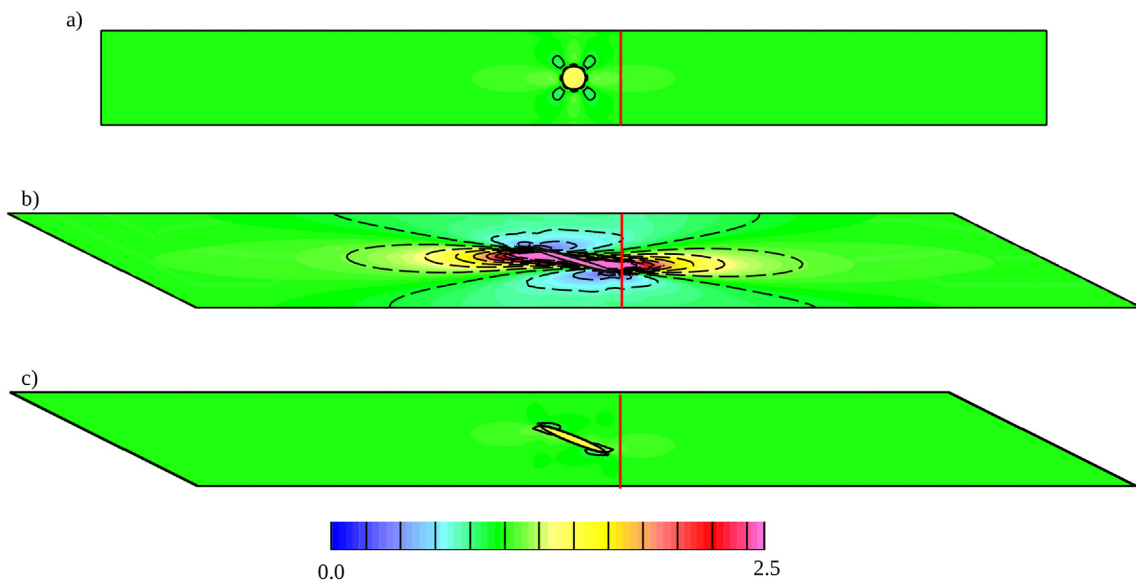


**Fig. 3.** The dimensionless maximum shear strain rate in the model at, a) onset of the applied boundary conditions, b) at total strain = 1 (with  $T_{ref} = 0.041$ ,  $\Lambda = 0.75$ ,  $n = 3$ , and  $\Gamma_0' = 1.0$ ), and c) at total strain = 1 ( $\Lambda = 0.75$ ,  $n = 3$ , and  $\Gamma_0' = 0$ ). Contour intervals at 0.2; colour saturates and contours are not shown for strain-rate  $> 2.5$ . Red line shows  $x' = 4$  (location of profiles in Fig. 4). (For interpretation of the references to colour in this figure legend, the reader is referred to the web version of this article.)

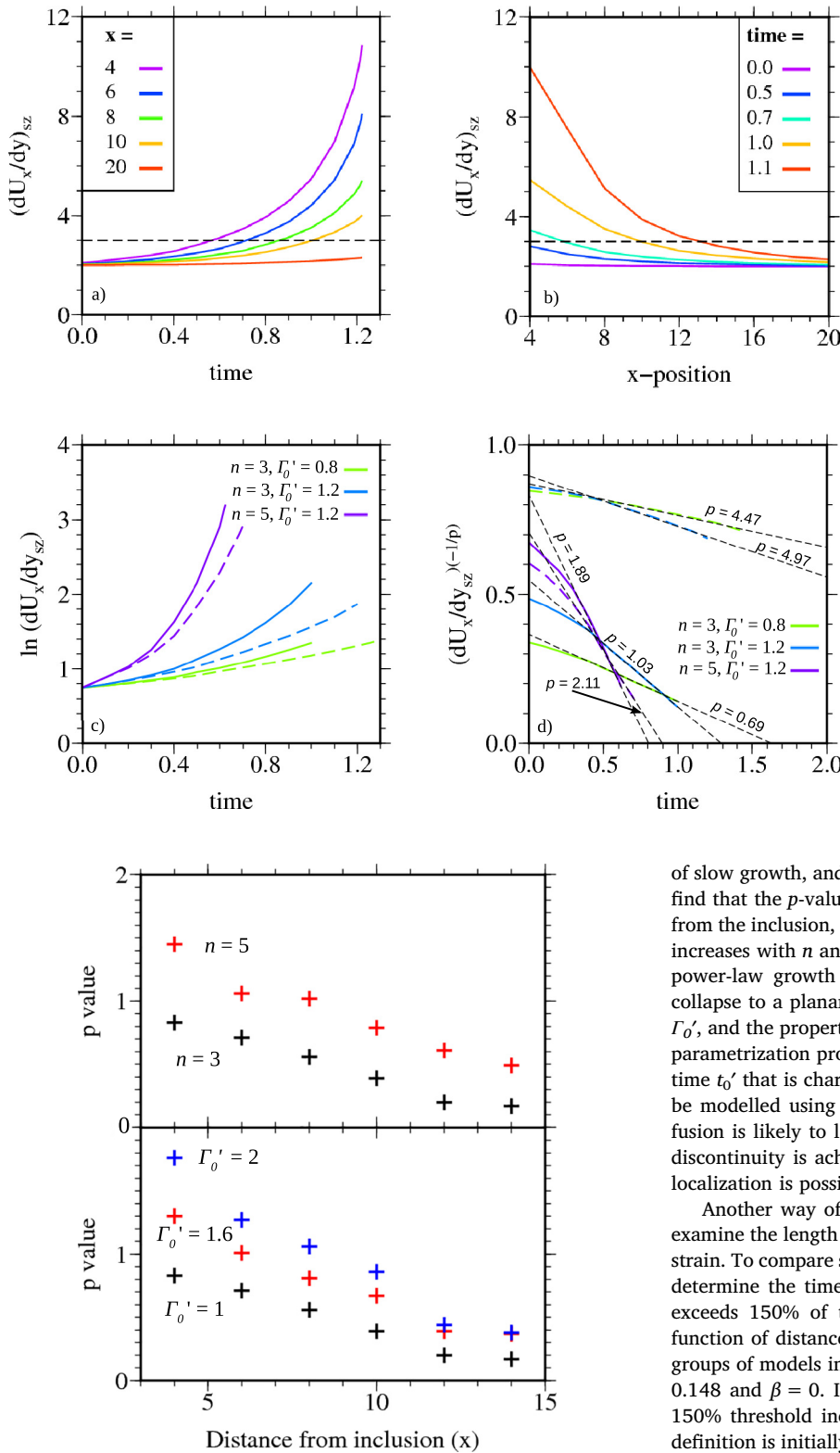


**Fig. 5.** a:  $\Lambda = 0.75$ ,  $n = 3$ ,  $\Gamma_0' = 1.0$ ,  $\beta = 0$ ,  $T_{ref} = 0.041$ ; velocity gradient  $dU_x/dy$  in the high-strain rate zone as a function of time for different values of  $x$ ;  $x = 4$  is closest to the inclusion and  $x = 20$  is furthest away. b: the same data plotted as a function of  $x$ -distance at different times. The dotted lines show when the velocity gradient in the shear zone exceeds 150% of the background velocity gradient. c:  $T_{ref} = 0.041$  (solid line) and 0.148 (dashed line) and other parameters as for (a); log-linear plot shows that initial shear zone gradient development is approximately exponential, but then increases at a rate greater than exponential, here shown for  $x = 4$  but this type of growth curve is observed at all distances from the inclusion. d: the same data as (c) projected to show that shear zone gradient evolves to follow a power law growth (Eq. (18)).

**Fig. 6.** For  $\Lambda = 0.75$ ,  $T_{ref} = 0.041$  and  $\Gamma_0' = 1$  with varying  $n$  (top) or  $n = 3$  with varying  $\Gamma_0'$  (bottom) the  $p$ -value from Eq. (18) with distance from the centre of the weak inclusion for  $x' \geq 4$ . The  $p$  values from the line of section that are initially closer to the weak inclusion are not calculated due to the progressively elongated weak inclusion crossing these regions, changing the velocity gradient measurement.

of slow growth, and the projected line intersects the time axis at  $t_0$ . We find that the  $p$ -values decrease systematically with increasing distance from the inclusion, from about 0.8 to about 0.2 (for  $n = 3$ ). The  $p$ -value increases with  $n$  and with  $\Gamma_0'$  (Fig. 6). The consequence of this type of power-law growth is that, in this idealized model, localization will collapse to a planar discontinuity in a finite time  $t_0$ , determined by  $n$ ,  $\Gamma_0'$ , and the properties of the initial heterogeneity (in this case  $\Lambda$ ). This parametrization provides a reasonable way to determine a localization time  $t_0$  that is characteristic of the localization process as far as it can be modelled using this method. In a geological scenario thermal diffusion is likely to limit this process well before the theoretical planar discontinuity is achieved, but we can still infer that a high degree of localization is possible for the same values of  $\Gamma_0'$ .

Another way of looking at the increase in strain localization is to examine the length of the shear zone as a function of increasing overall strain. To compare shear zone development in different experiments we determine the time at which the velocity gradient in the shear zone exceeds 150% of the background velocity gradient. This time is a function of distance from the weak seed, as shown in Fig. 7 for three groups of models in which  $\Lambda$ ,  $n$  or  $\Gamma_0'$  are varied with  $T_{ref} = 0.041$  and 0.148 and  $\beta = 0$ . In general the length of the zone that exceeds the 150% threshold increases linearly with time. The shear-zone by this definition is initially longer and grows faster for smaller  $\Lambda$  (Fig. 7a), for larger  $n$  (Fig. 7b), and for larger  $\Gamma_0'$  (Fig. 7c). For  $\Lambda = 0.5$  and 0.25 in Fig. 7a, distortion of the finite element mesh prevented our calculations from running further but we saw no evidence of departure from linearity in this measure. Although the shear-zone grows faster for  $\Lambda = 0.5$  and 0.25, the 50% increase in strain rate is still achieved for  $\Lambda = 0.75$  with  $n = 3$  and  $\Gamma_0' = 1.2$ .

In a similar set of experiments with  $\beta > 0$ , we investigated the impact of thermal diffusion on the shear zone formation (Fig. 8). As in Fig. 7 we determined the times at which the values of  $dU_x/dy$  in the

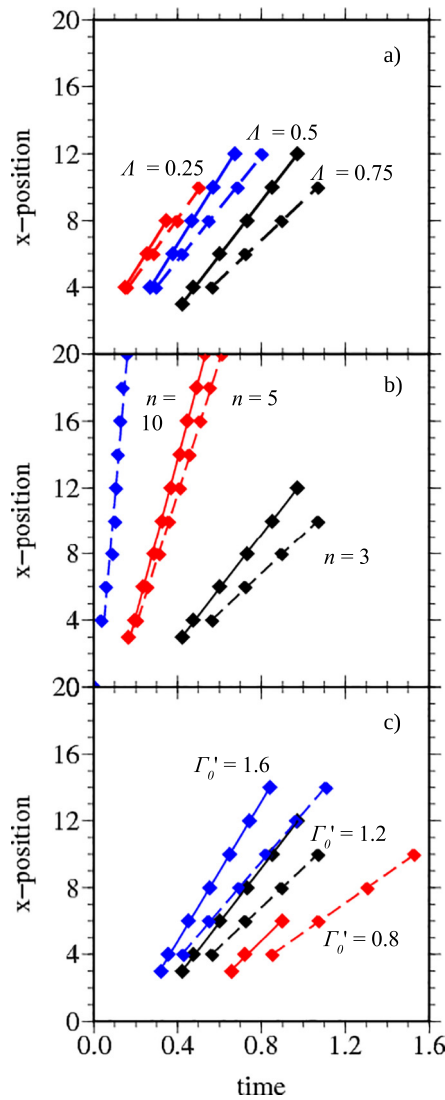


**Fig. 7.** Shear-zone extent vs time: for each  $x$ -value in an experiment, the time at which  $dU_x/dy$  in the high strain-rate zone exceeds 150% of the background strain-rate value is plotted for experiments with a)  $n = 3$ ,  $\Gamma_0' = 1.2$ ,  $\Lambda$  as labelled; b)  $\Lambda = 0.75$ ,  $\Gamma_0' = 1.2$ ,  $n$  as labelled; c)  $\Lambda = 0.75$ ,  $n = 3$ ,  $\Gamma_0'$  as labelled. Solid lines are for  $T_{ref} = 0.041$ , dashed for  $T_{ref} = 0.148$ ; in each case  $\beta' = 0$ . The high strain-rate zone does not exceed 150% of the background strain-rate when  $n = 1$ .

high strain-rate zone exceed 150% of the background rate. We find that the approximately linear relationship between shear-zone length and time is generally preserved, but an increase in  $\beta$  reduces the strain localization and increases the time required to reach the 150% threshold. For  $T_{ref} = 0.041$  and  $0.148$ , sufficiently large values of  $\beta$  ( $\sim 10$  for  $n = 3$  or  $5$ ) suppress the thermal localization of strain. For smaller values of  $\beta > 0$ , the initial period of exponential increase in localization is extended. In such cases it appears that the exponential rate of reduction in the work parameter  $D$  associated with  $\beta > 0$  in general is overwhelmed eventually by the power-law (Eq. (18)) increase caused by viscous heating, if  $\Gamma_0'$  is sufficiently large.

Kaus and Podladchikov (2006) showed that a visco-elasto-plastic deformation regime was capable of developing regions of reduced viscosity, dependent on a shear-heating efficiency parameter that is analogous to our  $\Gamma_0'$ . Our results are broadly consistent with theirs for large values of  $n$  (which can be considered an approximation for plastic behaviour) but we find that, for any value of  $n \geq 2$ , strong localization can develop for a background strain of  $\varepsilon_0' = 1$  when  $\Gamma_0'$  exceeds a

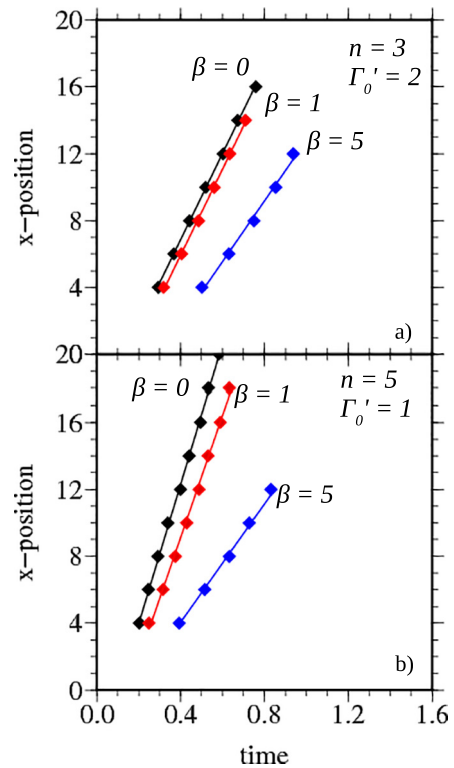


**Fig. 8.** Shear zone extent versus time (as defined in Fig. 7) for  $T_{ref} = 0.041$ ,  $\Lambda = 0.75$  and values of  $\beta'$  as labelled for a)  $n = 3$ ,  $\Gamma_0' = 2$  and b)  $n = 5$ ,  $\Gamma_0' = 1$ . Increasing  $\beta$  increases the time for strain to reach the 150% threshold or slows the growth of the shear zone. For  $\beta \geq 10$  the 150% threshold is not reached for either combination of parameters.

threshold value. This value depends on  $n$ ,  $T_{ref}$ ,  $\Lambda$ , and  $\beta'$ . Values of the time-scale for localization ( $t_0'$  in Eq. (18)) obtained from our numerical experiments are summarized by the contour plot in the  $n$ - $\Gamma_0'$  parameter space of Fig. 9 for two different values of  $T_{ref}$ . The value of  $\Gamma_0'$  required for a shear zone to localize within the time corresponding to a background strain of about 1 ( $t_0' = 1$ ) can then be read from Fig. 9 for a given  $n$  value. For  $n = 3$  to  $4$ , typical of silicates undergoing dislocation-creep deformation (Table 1),  $\Gamma_0' > 1.5$  produces localization on this time-scale for  $T_{ref} = 0.041$  (relevant to olivine or dry quartz, Fig. 9a). Where  $T_{ref} = 0.148$ , as for wet quartz, we extrapolate the graph to infer that localization occurs when  $\Gamma_0' > 2.5$  (Fig. 9b).

For  $n = 1$  localized regions of high shear strain rate do not develop, even if  $\Gamma_0'$  is as high as 50 and  $\Lambda$  is as low as 0.25. Consequently in this model for which strain-weakening depends on thermal activation, a non-Newtonian (power-law) rheology appears necessary to the development of significant strain-localization. Localized deformation is inhibited (i.e. the high-strain regions do not exceed 150% by  $t' = 1$ ) where  $\Gamma_0' \leq 0.3$  for  $n$  up to at least 10.

Our results demonstrate that for,  $\Gamma_0' > 0.3$ , lithospheric silicate minerals are capable of a high degree of localization if strain is sufficiently rapid that thermal diffusion can be neglected. Where thermal diffusion is significant ( $\beta > 0$ ), localization can still occur for a greater value of  $\Gamma_0'$  but, where diffusion is sufficiently high, localization is suppressed, as Kaus and Podladchikov (2006) showed for 1D viscous deformation models. Although localization in our idealized model with  $\beta = 0$  can see the shear-zone collapse into a planar discontinuity conceptually similar to a fault, thermal diffusion will generally prevent that outcome in a real silicate because the decreasing width of the shear zone causes  $\beta$  to increase as the localization progresses.

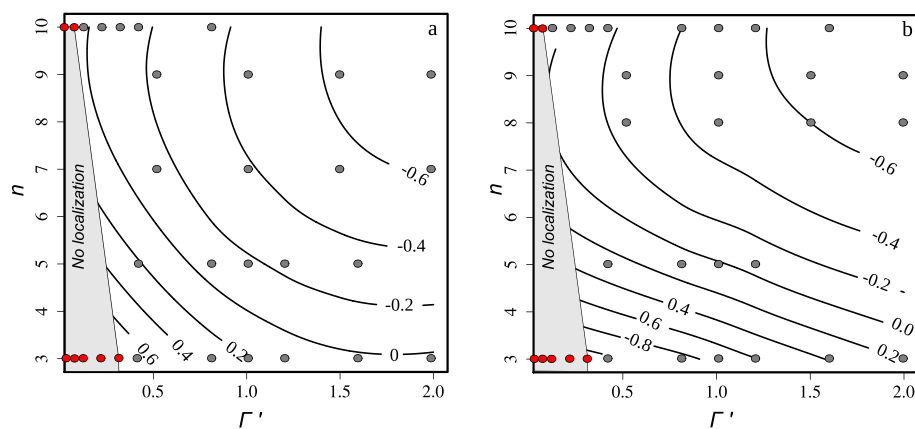


**Fig. 9.** Gridded and contoured values of  $\log_{10}(t_0')$  obtained from the type of analysis shown in Fig. 5d, using measurements at  $x = 4$  for experiments with  $\Lambda = 0.75$  and  $T_{ref} = 0.041$  (a) or  $0.148$  (b). Grey circles indicate numerical experiments in which localization occurs, red circles indicate no localization. For  $n = 3$  or  $4$  (most relevant to silicates deforming by dislocation creep) these maps show that  $t_0' < \text{about } 1$  (i.e. strain is localized within the time interval required for a strain of 1) if  $\Gamma_0' > \text{about } 1.5$  (for  $T_{ref} = 0.041$ ) or about  $2.5$  (for  $T_{ref} = 0.148$ ). The interval  $t_0' = 1$  corresponds to  $t_0 = 3$  Myr for a strain rate of  $10^{-14} \text{ s}^{-1}$ . Results for  $n = 1$  are not shown here, but in experiments with  $\Gamma_0'$  up to  $50$  no significant localization was observed. (For interpretation of the references to colour in this figure legend, the reader is referred to the web version of this article.)

#### 4. Strain localization with depth

In the preceding section of this paper we have considered how localized deformation within a 2D horizontal section of the lithosphere may develop when that section is subject to a simple-shear deformation representative of a strike-slip environment in the lithosphere. We now consider how that development may vary with depth within the lithosphere, recognising that temperature, pressure and lithology vary systematically with depth but that the entire lithospheric section is exposed to the same background strain rate. This approach obviously neglects the interaction between different depths, in order that understanding might be developed without the complexity of a comprehensive 3D thermo-mechanical solution. The lithology, temperature, and pressure enter this analysis because they control the background viscosity coefficient in our 2D deformation experiments. Our dimensionless formulation of the problem in Section 2 allows us to directly interpret that variation of background viscosity as a variation of the dimensionless parameter  $\Gamma_0'$  used in the preceding numerical experiments.

A lithosphere-scale fault zone is typically depicted as a localized fault plane in the upper lithosphere above a ductile shear zone whose width increases with depth in the mid to lower lithosphere (e.g. Burgmann and Dresen, 2008; Moore and Parsons, 2015; Vauchez et al., 1998). We show here that this qualitative understanding of fault-zone structure is consistent with our thermal localization analysis which predicts that there is a maximum temperature and depth at which a shear zone can localize. This depth is dependent on strain-rate, heat-flow and mineralogy.

To evaluate the relevant dimensionless value of  $\Gamma_0'$  (Eq. (17)) for a given lithology at a particular depth we need estimates of background strain rate, temperature, pressure, and water fugacity (where relevant). These background values are based on a 1D two-layer model of crust over mantle with a steady-state conductive geothermal in which the top and bottom temperatures are constrained to be  $20^\circ\text{C}$  and  $1350^\circ\text{C}$  respectively and we adjust the radioactive heating in the crust to give a prescribed surface heat flow ( $F$ ). In doing so we assume an upper crustal layer to  $18$  km depth in which the heat production is twice that of a lower crustal layer to  $40$  km depth and thermal conductivity for crust and mantle of  $2.5$  and  $3.0 \text{ W m}^{-1} \text{ K}^{-1}$  for crust and mantle respectively. The calculation of pore-fluid pressure assumes a lithostatic profile with typical crustal and mantle densities of  $2700$  and  $3300 \text{ kg m}^{-3}$ , and we calculate  $f\text{H}_2\text{O}$  following the method of Pitzer and Sterner (1994) and Sterner and Pitzer (1994) assuming lithostatic pore fluid pressure. The background strain-rate is assumed constant with depth. Using plausible background tectonic strain-rates in the range  $10^{-16}$  to  $10^{-13} \text{ s}^{-1}$ , equilibrium geotherms for heat flow in the range  $40$  to  $100 \text{ mW m}^{-2}$ , and published rheological constants for quartz, plagioclase and olivine (Hirth and Kohlstedt, 2013; Hirth et al., 2001; Rutter and Brodie, 2004;

Rybacki and Dresen, 2000), we calculate how  $\Gamma_0'$  (Eq. (17)) varies with depth in the lithosphere (Fig. 10).

We have shown (Fig. 9) that localization proceeds very rapidly for values of  $\Gamma_0'$  that are not much  $> 1.5$  (for  $T_{ref} = 0.041$ , representative of olivine) or  $2.5$  (for  $T_{ref} = 0.148$ , representative of wet quartz), and Fig. 10 shows that  $\Gamma_0'$  varies by orders of magnitude with depth in the lithosphere, due mainly to a strong dependence of the rheological laws on temperature. The characteristic  $\Gamma_0'$  profiles shown in Fig. 10 thus imply that we should expect localization to occur at shallower levels in the lithosphere. Furthermore, for any given lithology, there is a depth below which thermal strain localization cannot occur, even in the absence of thermal diffusion. Although there may be significant uncertainty in the maximum localization depth due to uncertain mineralogy, water fugacity, surface heat-flow and background strain-rate, the uncertainty arising from the choice of threshold value of  $\Gamma_0'$  is small. In Fig. 10 we see that changing the threshold  $\Gamma_0'$  value from  $1.5$  to  $2.5$  decreases the maximum localization depth in olivine by  $2$  to  $3$  km.

Deformation in the continental upper crust is often assumed to be represented by the flow law for quartz. In the lower crust the decreasing abundance of quartz with depth suggests that deformation is increasingly accommodated by plagioclase. We therefore show (Fig. 10)  $\Gamma_0'(z)$  for both of these minerals down to a nominal crustal thickness of  $40$  km. Within the lithospheric mantle, olivine rheology is assumed to control deformation, so we show  $\Gamma_0'(z)$  for olivine within the mantle layer. In each layer we show  $\Gamma_0'(z)$  for both “dry” and “wet” rheological laws, using parameters in Table 1.

Assuming a lithostatic pore-fluid pressure, a quartz-dominated lithology will localize above a depth (Fig. 10c–f) that may be as shallow as  $5$  km (fugacity dependent,  $F = 100 \text{ mW m}^{-2}$ ,  $\dot{\epsilon} = 10^{-16} \text{ s}^{-1}$ ) or as deep as  $30$  km (dry conditions,  $F = 40 \text{ mW m}^{-2}$ ,  $\dot{\epsilon} = 10^{-13} \text{ s}^{-1}$ ). Plagioclase supports a greater stress at the same strain-rate, and hence localization can occur at deeper levels in the crust, as shallow as  $14$  km (hydrous conditions,  $F = 100 \text{ mW m}^{-2}$ ,  $\dot{\epsilon} = 10^{-16} \text{ s}^{-1}$ ) and as deep as  $60$  km (dry conditions,  $F = 40 \text{ mW m}^{-2}$ ,  $\dot{\epsilon} = 10^{-13} \text{ s}^{-1}$ ). For typical Moho depths of around  $40$  km, plagioclase therefore is capable of localizing strain throughout the lower crust, but does not do so where surface heat flow is relatively high and strain-rate relatively low. Within the mantle lithosphere we see a similar range of behaviours for an olivine-dominated lithology (Fig. 10c–f); at one extreme (fugacity dependent,  $F = 100 \text{ mW m}^{-2}$ ,  $\dot{\epsilon} = 10^{-16} \text{ s}^{-1}$ ) the transition depth for localization is at  $22$  km, implying that localization should not be expected in the upper mantle of normal continental crust. However, localization depth increases if surface heat flow is decreased or strain-rate is increased, with localization possible to  $64$  km depth under dry conditions with  $F = 40 \text{ mW m}^{-2}$  and  $\dot{\epsilon} = 10^{-13} \text{ s}^{-1}$ . Strain-localization in the upper-most part of the continental mantle lithosphere should therefore be expected in regions of lower heat-flow and greater strain-rate, especially in the absence of significant fluid content.

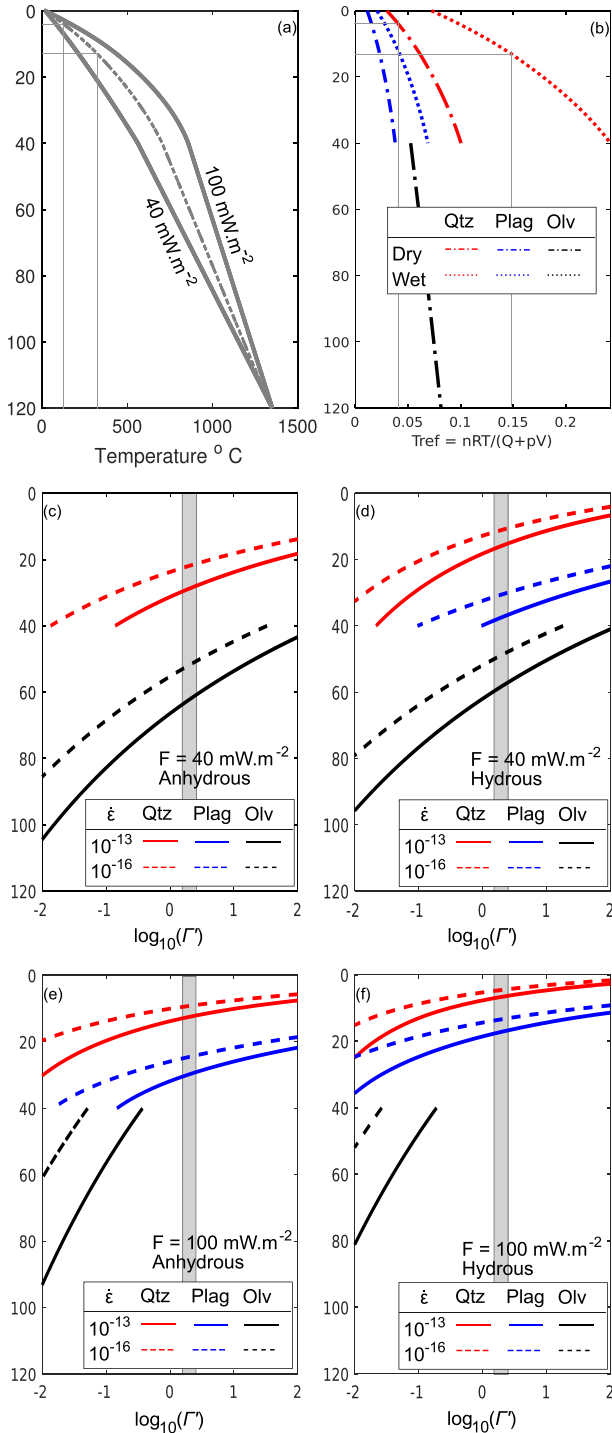


**Fig. 10.** a) Calculated geotherms for surface heat-flow  $F = 40, 70$  and  $100 \text{ mW}\cdot\text{m}^{-2}$ . (b) Values of  $T_{ref}$  for  $F = 70 \text{ mW}\cdot\text{m}^{-2}$  derived from Eq. (11) for dry and wet conditions, with fugacity for quartz and olivine derived for a lithostatic fluid pressure. Representative  $T_{ref}$  values used in numerical experiments (Section 3, Table 1) are shown here by thin grey lines, with the corresponding temperature for the depth where  $F = 70 \text{ mW}\cdot\text{m}^{-2}$  shown on panel a. For olivine (black) the  $T_{ref}$  values are near identical for dry and fugacity dependent rheology. For c), d), e) and f), with  $F$  as labelled, strain-rate =  $10^{-13} \text{ s}^{-1}$  (solid lines) and  $10^{-16} \text{ s}^{-1}$  (dashed), c) and e) show  $\log_{10}(I')$  vs depth for dry mineral conditions, and d) and f) show same for fugacity dependent (quartz and olivine) and wet (plagioclase) lithology. The grey band shows the threshold values obtained from Fig. 9 for localization to occur with  $t_0' < 1$ , i.e.,  $\log_{10}(I') = 0.18$  for  $T_{ref} = 0.014$  and  $\log_{10}(I') = 0.40$  for  $T_{ref} = 0.148$ . For c) the values of  $\log_{10}(I')$  for plagioclase plot to the right of the graph, so localization is expected for the entire crustal depth range.

In each lithology that we consider, the maximum depth of localization deepens with increasing background strain-rate and shallows for increasing surface heat-flow, as summarized in Fig. 11. Older, cooler lithosphere may show a greater depth of localization but the increase in depth may be moderated by slower strain-rates. On the other hand, tectonic environments such as rifts and established orogens typically have a high surface heat flow and the localization will not be as deep, even allowing for the typically greater strain rates in such regions.

The distribution of aqueous fluids in the lithosphere is likely to be heterogeneous but a broad inference can be made on specific settings. For example, metamorphic rocks that have been exposed to high pressures and temperatures have an insignificant fluid content, but sedimentary basin settings see a high fluid content (Yardley and Bodnar, 2014). Where minerals contain water there is a significant decrease in the depth of localization (Fig. 11). For  $F = 80 \text{ mW}\cdot\text{m}^{-2}$  and  $\dot{\epsilon} = 10^{-13} \text{ s}^{-1}$  a change from dry to 0.07 wt%  $\text{H}_2\text{O}$  in plagioclase moves the maximum depth of localization from 40 to 23 km, that is a rheology controlled by wet plagioclase does not allow localization within the lower continental crust. Under the same surface heat-flow and strain-rate conditions, dry olivine will localize below typical Moho depths ( $\sim 46 \text{ km}$ ). However, if the increase of water fugacity in a hydrous environment is accounted for, the maximum potential localization depth in olivine is  $\sim 35 \text{ km}$ , shallower than typical Moho depths, thereby suppressing shear localization in the upper mantle.

Although we neglect thermal diffusion in this simplified analysis ( $\beta = 0$ ), we recognise that the final stages of the localization instability will be limited in reality by diffusion of heat away from the progressively narrowing shear zone. Where deformation is slow thermal diffusion is likely to inhibit shear zone formation completely.

## 5. Discussion: comparison with major strike-slip faults

We now examine geophysical data from two major continental strike-slip shear zones that show differences in surface-heat flow (and hence geothermal gradient) and slip-rate: the San Andreas and North Anatolian Fault zones. We compare the evidence for localization of deformation at depth within these shear zones with our estimates of maximum shear localization depth. Evidence of localization within the crust beneath active strike-slip systems comes primarily from seismology, whether in the occurrence of microseismicity and seismic tremor, or seismic imaging that shows offset structure. Because the activation of localization occurs over a relatively narrow depth range dependent on the rheological and environmental parameters, evidence for or against shear localization at a given depth may place constraints on lithology and water-content in that environment.

For each of these regions, published bore-hole data provide estimates of the surface heat-flow, which constrains the geothermal gradient used in the strain localization calculations. We also require an estimate of the background strain-rate across each of these shear zones. Interseismic geodetic data show in general a well-defined zone of continuous deformation typically 40 or 50 km wide either side of these active strike-slip faults, as recently summarized by Wright et al. (2013). This is the surface expression of distributed deformation below the seismogenic layer, filtered through the elastic lid, and is often described using the simplified conceptual idea of an elastic plate overlying a buried dislocation on which movement occurs at the plate rate  $\dot{s}$  below locking depth  $d$  (Savage and Burford, 1973; Segall, 2002). The measured surface deformation actually cannot distinguish between slip on a fault below depth  $d$ , and distributed shear across a ductile zone of width  $\pi d$  (Moore, 1999), and in fact the latter is physically more plausible. Thus the same geodetic motion might be indicative of a localized, brittle deformation, or a distributed deformation. We assume, in the absence of more definitive data, that this observed strain-rate:

$$\dot{\epsilon}_0 = \frac{\dot{s}}{2\pi d} \quad (19)$$

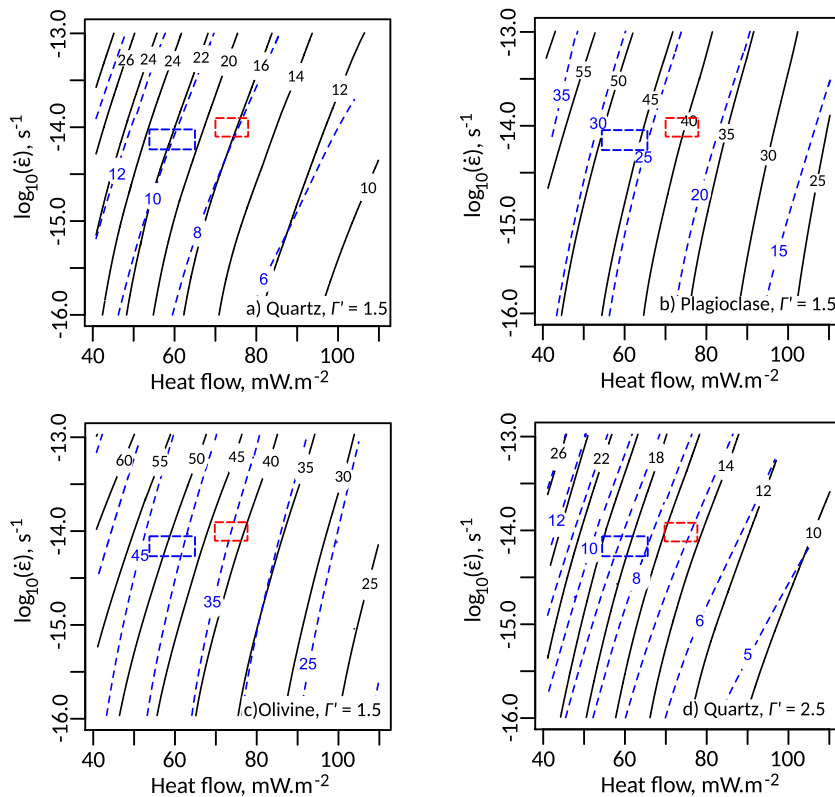


**Fig. 11.** Gridded and contoured values for depth (km) at which  $\Gamma' = 1.5$  (a, b, c) or 2.5 (d) as a function of surface heat flow and strain-rate, based on interpolation of profiles like those shown in Fig. 10. Black solid contours indicate dry mineral conditions and blue dashed contours indicate fugacity dependent (quartz, olivine) or wet (plagioclase) minerals. The red and blue boxes show the estimated ranges of surface heat-flow and strain-rate for the SAFZ and NAFZ respectively (refer text), from which a maximum depth of localization can be inferred for each lithology. (For interpretation of the references to colour in this figure legend, the reader is referred to the web version of this article.)

is indicative, and plausibly represents a minimum estimate, of the background strain-rate across the deforming region in the ductile layer below the elastic lid.

We allow for a 25% uncertainty on our estimate of the background strain-rate in order to show the influence of uncertainty in this parameter. We note however, that strain-rate (raised to the power of  $1/n$  in Eq. (17)) has less effect on  $\Gamma'_o$  (and hence on the maximum depth of localization) than mineralogy, presence of fluids or heat-flow, as is evident from Fig. 11.

The San Andreas Fault Zone (SAFZ) is a dextral strike-slip system on which the relative motion of the Pacific and North American plates is localized. Geodetic data define a relative strike-slip motion across the central SAFZ of about 38 mm/yr (Prescott et al., 2001). Surface deformation is distributed across a near-fault zone that is highly variable in width (Titus et al., 2011). This variability is captured in the locking depth which varies from 6 to about 22 km (Smith-Konter et al., 2011). For a locking depth of 20 km, (e.g. Segall, 2002; Shen et al., 1996) with a nominal 25% uncertainty, the relevant background strain rate is in the range  $0.8$  to  $1.3 \times 10^{-14} \text{ s}^{-1}$ . Borehole heat-flow measurements of the central SAFZ range from 54 to 92  $\text{mW}\cdot\text{m}^{-2}$  and the mean measurement is  $74 \pm 4 \text{ mW}\cdot\text{m}^{-2}$  (Sass et al., 1997). Given these estimates of strain-rate and heat flow, we can use Fig. 11 to infer the expected average maximum depth of shear localization for typical lithospheric lithologies. To simplify, we again consider our two representative values of  $T_{\text{ref}}$ . For dry quartz, and all plagioclase and olivine  $T_{\text{ref}} = 0.041$  is more relevant and maximum localization depths inferred are 16 km for dry quartz (Fig. 11a), 23 (wet) to 41 km (dry) for plagioclase (Fig. 11b) and 35 (wet) to 42 km (dry) for olivine (Fig. 11c). For wet quartz dominated lithologies at higher temperatures, we infer from the greater value of  $T_{\text{ref}} = 0.148$  (Fig. 11d) a maximum depth of shear localization of 7 km.

Lower limits on the depth of strain-localization are clearly indicated by the spatial distribution of micro-seismicity. A regional study of crustal seismicity in southern California by Nazareth and Hauksson (2004) determined seismogenic thickness varying locally between  $\sim 10$

and  $\sim 25$  km, with an average about 15 km. Other evidence for the extent of localization depends on the locking depth estimate (as previously mentioned) and structural information derived from seismic imaging. Tomographic inversions for crustal velocity variation in regions that encompass parts of the SAFZ (Allam and Ben-Zion, 2012; Chen et al., 2007; Lin et al., 2007; Thurber et al., 2004) often show a well-defined sharp velocity contrast across the SAFZ that is consistent with localized deformation continuing to a depth of 15 km or more (Thurber et al., 2006) but in general resolution is poor below about 15 km because the tomographic solutions are constrained by local earthquakes that are generally shallower than that depth. Thus the style of deformation in the lower crust is not well constrained by seismological measurements. However, the receiver function method, based on converted waves from teleseismic sources, does provide some important clues about deformation at the Moho. Following Zhu (2000), Yan and Clayton (2007) inferred an increase in Moho depth from 29 to 32 km on the San Gabriel side to 35–40 km on the Mojave side of the San Andreas Fault, implying that the SAF cuts right through the crust. Ozakin and Ben-Zion (2015) also found comparably large vertical offsets in the Moho, and associated significant changes in Moho depth with fault complexity in the brittle crust. Although the lateral resolution of the receiver function method is probably no better than 5 or 10 km, the inferred step in the Moho suggests that deformation associated with the SAFZ is localized in the uppermost mantle. The adjacent lowermost crust of course must have a comparable deformation, but whether localization is independently maintained through the lower crust is difficult to assess from the available imaging data. At greater depths there are few constraints, but an S to P receiver function profile across the central (Parkfield) section of the SAFZ by Ford et al. (2014) shows, at  $\sim 60$  to 80 km depth, some variation in the velocity structure occurring over a horizontal distance of  $\sim 50$  km; they interpreted an offset in the lithosphere-asthenosphere boundary related to the fault system. The horizontal resolution of such methods certainly does not preclude the possibility of a localized shear zone reaching depths of 60 or 80 km, but the resolution of the width measurement is also consistent with a low

degree of shear localization at the base of the lithosphere.

The geophysical evidence supports localization of the SAFZ in the upper crust and at the Moho, consistent with the predictions of our simplified model, but does not clearly constrain the degree of localization within the lower crust. Localization throughout the lower crust could be explained by thermal activation of a plagioclase-dominated lithology if water is absent (Fig. 11b). For a quartz-dominated lithology we do not expect to see thermally-activated localization deeper than about 16 km under dry conditions, while localization should be limited to depths < 10 km if water is present. The seismic observations that localization probably extends to 15 km or more at the SAFZ therefore suggests that either the mid-crust is dry or its rheological law is better represented by that of plagioclase (for which, even if wet, we expect localization to ~23 km) than quartz. The presence of fluid alteration minerals to a depth of 3 km within the San Andreas Fault Observatory at Depth (SAFOD) borehole indicates hydrous conditions within the upper crust (Bradbury et al., 2011; Holdsworth et al., 2011). If hydrous conditions are maintained in the depth range of 10 to 20 km below the SAFZ we infer that a rheological law representative of plagioclase applies in this depth range. If hydrous conditions persist into the lower crust we would not expect shear zone formation to occur below about 23 km depth.

The evidence for localization in the mantle lithosphere at depths greater than about 50 km is also ambiguous, as the observed lithosphere-asthenosphere boundary offset inferred from S to P receiver functions (Ford et al., 2014) occurs over a region whose width is comparable to the horizontal resolution of the imaging method (~50 km). However the apparent structural discontinuity at the Moho, from estimated depth of 30 km to 38 km (Zhu, 2000) is consistent with the thermally activated strain localization in a dry olivine-dominated lithology, for which our model implies a maximum depth of localization of 42 km. Acceptance of shear zone localization in the uppermost mantle therefore can be taken as evidence that the uppermost mantle is dry in this region (Fig. 11c).

We now consider the North Anatolian Fault zone (NAFZ), a dextral, strike-slip fault system in northern Turkey that accommodates relative movement of the Eurasian and Anatolian plates and is in many ways comparable to the SAFZ. Geodetic measurements estimate a strike-parallel relative velocity across the NAFZ of 24 mm/yr (Hussain et al., 2018; McClusky et al., 2000). Using the same GPS data Yamasaki et al. (2014) showed a profile across the NAFZ at ~30.25°E for which a shear zone width of ~50 km is apparent, consistent with the locking depths of 16 to 17 km derived by Hussain et al. (2018).

Variation of the shear-zone width along the NAFZ is probably comparable to that along the SAFZ and, although multiple studies have been made of the fault segments that are still affected by after-slip from the 1999 earthquakes at Izmit and Duzce, the pre-seismic strain-rate field is less well constrained by data than is that of the SAFZ. Again assuming a 25% uncertainty we estimate the background strain-rate for the NAFZ between 6 and  $10 \times 10^{-15} \text{ s}^{-1}$ . This estimate is about 30% less than that for the SAFZ, mainly because the far-field plate-motion rate is ~24 mm/yr rather than ~38 mm/yr. Terrestrial heat flow in the region cut by the NAFZ is highly variable because of groundwater flow. From borehole data (Pfister et al., 1998) north of 40° N the mean heat flow is  $60 \pm 5 \text{ mW m}^{-2}$ . These measurements constrain only the western end of the NAFZ. In the context of Fig. 11, the NAFZ environment is characterized by both lower heat flow and lower strain-rate than that of the SAFZ and when  $T_{\text{ref}} = 0.041$  the maximum depth of strain localization is therefore increased by ~5 km for each lithology, to 22 km (Fig. 11a) for dry quartz, to 27 (wet) to 48 km (dry) for plagioclase (Fig. 11b), and to 42 (wet) to 49 km (dry) for olivine (Fig. 11c). For wet quartz we use  $T_{\text{ref}} = 0.148$  (Fig. 11d) and infer a maximum depth of shear localization of 9 km.

Comparable to the SAFZ, a seismogenic depth of ~15 km was obtained from the DANA seismic array on a western segment of the NAFZ (Altuncu-Poyraz et al., 2015). However, geophysical images may

support a greater depth of strain localization. Tomographic models based on analysis of local seismic event records show  $V_p$  variation beneath the northern branch of the NAFZ (NNAF) (Baris et al., 2005; Salah et al., 2007; Yolsal-Çevikbilen et al., 2012). Yolsal-Çevikbilen et al. (2012) show north-south vertical sections (near perpendicular to the fault) in which positive  $V_p$  anomalies extend beneath the NNAF. The geometry of the anomalies varies along strike, likely due to pre-existing crustal heterogeneities, but this method is subject to decreasing resolution in the lower crust. Papaleo et al. (2017), however, used teleseismic events detected by a high density seismic array over the fault segment that ruptured in 1999, and claimed a horizontal and vertical resolution of less than about 15 km (though less well resolved below about 40 km depth). They show a zone of low  $V_p$  that extends to about 80 km depth. The width of the low  $V_p$  zone is relatively localized in the upper crust (~25 km), but it increases to perhaps 50 km in the upper mantle, comparable to the estimate of Ford et al. (2014) for the width of the SAFZ shear zone at the base of the lithosphere. In either case the imaging method would have difficulty in resolving a narrower structure at the lithosphere-asthenosphere boundary. The receiver function method (Kahraman et al., 2015) suggests a localized shear zone below the NNAF at 30 to 30.5°E, where horizontal interfaces in the crust and upper mantle are truncated beneath both strands of the NAF. The lateral resolution of this method at the Moho is about 10 km and increases linearly with depth in the mantle. Their north-south profile across the NAFZ at 30.2°E shows a positive anomaly horizon at ~34–39 km depth, interpreted as the Moho. Beneath the NNAF the amplitude of the arrival decreases, suggesting a more gradational velocity contrast across the Moho at this location, without a clear offset of Moho depth. Autocorrelation of ambient seismic noise data by Taylor et al. (2016) shows an absence of P wave reflectivity at Moho depths within 7 km of the NNAF, but they interpret distinct offsets of the Moho within about 10 km of the NNAF strand. They attributed the absence of a reflector in the autocorrelation below the NNAF to serpentinisation of olivine in the uppermost mantle producing a more gradational velocity variation across the Moho.

The geophysical evidence of localization occurring throughout the crust in the NAFZ region is consistent with our calculations for a thermally activated regime with a plagioclase dominated lithology in the lower crust. Referring again to Fig. 11 for the prevailing strain-rate and thermal conditions relevant to the NAFZ, we predict for a quartz dominated lithology that localization is limited to depths less than ~9 km (wet) or ~22 km (dry), contrary to the apparent localization indicated by discontinuous crustal boundaries in the receiver function sections of Kahraman et al. (2015). For a plagioclase lithology, however, even with fluid present a maximum localization depth of ~27 km is expected. The seismic evidence for localized deformation in the lower crust is not entirely clear but a dry plagioclase lithology would allow localization of the deformation to extend through the crust. If water is also assumed to be absent in the upper mantle then the olivine dominated lithology in our model would predict a maximum localization depth of ~49 km, consistent with evidence of localized deformation at the Moho. Thus, for both SAFZ and NAFZ we do not expect localization to extend to the base of the lithosphere. In both regions however, the robustness of these inferences regarding lithology and role of fluid, would benefit from improved resolution of the seismically imaged shear zones within the lower crust and uppermost mantle.

In considering the possibility of a thermal localization method in a sheared silicate mass, we have not dwelt on the relationship between what are evidently faults at near-surface levels and shear-zones of varying width at deeper levels. Faults produced by brittle fracture may propagate downward to form shear zones that extend to deeper levels. Conversely, localized shear at the deeper levels may precede, facilitate and organize faulting at the shallower levels. The two processes are likely interlinked, but it is unlikely that shear zones will develop only because of overlying fault systems, unless there is an intrinsic feedback mechanism which progressively weakens the undeformed mass. It is

notable that major strike-slip shear zones, such as the San Andreas and North Anatolian fault zones, extend across tens of km and typically involve a surface network of anastomosing faults contained within the shear zone (e.g., Sengor et al., 2005). It is also noteworthy that the shear localization model described here predicts that the length of the shear zone increases linearly with increasing strain, just as maximum fault displacement increases with length of fault (Cowie and Scholz, 1992). Our inferences regarding a maximum depth of localization are broadly consistent with those of Yuen et al. (1978) in that both approaches show that crustal-scale shear zones are consistent with thermally activated models of lithospheric rheology. Yuen et al. (1978) also established that increasing background temperature suppresses localization, though they concluded that thermally activated shear zones might be stable to depths of 100 km or more, whereas we do not expect localization to be stable to depths greater than about 60 km (Fig. 11). This difference might be explained by their presupposing that a stable 1D structure is possible, whereas we have approached the question by asking whether a shear zone can grow from a point heterogeneity. The two approaches are complementary ways to view a complex problem.

In calculating the maximum localization depth we have considered only a shear-heating weakening mechanism. Comparison of these results with seismic data interpretations, suggests that shear-heating can be an important localization mechanism in the lithosphere. Our results do not consider thermal diffusion, and so may over-estimate the depth to which a thermal weakening localization mechanism is possible. Other strain-weakening mechanisms, such as grain-size reduction, may account for localization in some circumstances (e.g. Precigout et al., 2007) but, for a sufficiently cool geotherm, grain-size sensitive deformation mechanisms are not thought to be relevant in the crust or upper levels of the mantle-lithosphere (Karato and Wu, 1993).

## 6. Conclusion

In considering deformation of the continental lithosphere we have shown that a region with a weak inclusion subjected to simple-shear can develop localized zones of high strain-rate near parallel to the direction of shear. A strain-weakening mechanism dependent on the mechanical work done by deformation enhances local strain and promotes further localization. The work done generates heat that locally raises the temperature of the thermally activated silicate. The strain rate in the shear zone follows a power-law growth curve, whose exponent  $p$  is dependent on the inclusion strength ( $A$ ), strain exponent ( $n$ ), initial strain-weakening parameter ( $\Gamma_0'$ ) and the rate at which it changes ( $T_{ref}$ ) with temperature, and the distance from the inclusion. If the strain-rate is sufficiently slow that cooling occurs, the onset of the

## Appendix 1

Here we provide more detail on the derivation of Eq. (12) from the integration of Eq. (6). In this step we consider plane-strain deformation at a constant depth. We therefore can assume  $A$ ,  $f_{H_2O}$  and  $s$  are constant and rewrite Eq. (4) as:

$$\ln\left(\frac{B}{G}\right) = \frac{Q + pV}{nRT} \quad (\text{A1-1})$$

where  $G$  includes all the other factors in Eq. (4). Squaring both sides of (A1-1), we use Eq. (7) to introduce  $\Gamma$ :

$$\left[\ln\left(\frac{B}{G}\right)\right]^2 = \left(\frac{Q + pV}{nRT}\right)^2 = \left(\frac{Q + pV}{nRT^2}\right)\left(\frac{Q + pV}{nR}\right) = \Gamma\rho C_p\left(\frac{Q + pV}{nR}\right) \quad (\text{A1-2})$$

And hence:

$$\Gamma = \left[\ln\left(\frac{B}{G}\right)\right]^2 \frac{1}{\rho C_p} \left(\frac{nR}{Q + pV}\right) \quad (\text{A1-3})$$

Substituting Eq. (A1-3) into Eq. (9) to give:

$$\frac{dB}{B} = \frac{-1}{\rho C_p} \left(\frac{nR}{Q + pV}\right) \left[\ln\left(\frac{B}{G}\right)\right]^2 dD \quad (\text{A1-4})$$

thermal localization instability can be delayed or suppressed.

Using published rheological models for the deformation of quartz, plagioclase and olivine, and strain weakening based on shear heating, we have shown that there is a threshold depth in the lithosphere below which shear does not localize. For these silicates undergoing dislocation-creep with  $n = 3$  or 4 a strain-weakening parameter  $\Gamma_0' > 1.5$  produces geologically rapid localization. For a range of representative geotherms, plausible strain-rates, and assumptions of fluid pressure, we calculated how the thermally activated strain-weakening parameter  $\Gamma_0'$  varies with depth in the lithosphere. Lithology is the principal control on localization depth, with quartz, plagioclase and olivine successively localizing to a greater depth. For a given strain rate and geotherm, a dry lithology localizes to a greater depth than a hydrous one. Localization depth increases with strain-rate and shallows for an increase in surface heat-flow, but changes in surface heat flow are the dominant influence. Localization in olivine to sub-Moho depths is possible, dependent on the crustal thickness, surface heat-flow and strain-rate and appears to be established in the case of two major strike-slip fault zones, both by the model predictions and by the seismic images, but localization of lithospheric deformation is not predicted to occur at depths greater than about 60 km.

For each of the San Andreas Fault Zone (SAFZ) and North Anatolian Fault Zone (NAFZ) we estimated surface heat-flow measurements and calculated strain-rates from geodetic studies. Under these conditions we do not expect localization in a hydrous quartz-dominated upper crust below about 10 km. Therefore seismicity to 20 km is more consistent with a dry quartz rheology, but is also possible with a hydrous plagioclase lithology. Localized shear within the lower crust is expected only if a dry plagioclase lithology applies. Similarly we do not expect well-developed strain localization in the upper-most mantle for a hydrous olivine lithology whereas a dry olivine lithology can explain the penetration of these major strike-slip shear zones into the uppermost mantle. The inference from seismic images of localized offsets on the Moho therefore implies that the uppermost mantle lithosphere is dry beneath these fault zones.

## Acknowledgements

This work was supported by Natural Environment Research Council (NERC) grant Looking Inside Continents from Space (NE/K010867/1). COMET is the NERC Centre for the Observation and Modelling of Earthquakes, Volcanoes and Tectonics. We thank two anonymous reviewers whose comments have led to significant improvements of the paper.

And defining for convenience in the following manipulation:

$$H = \frac{1}{\rho C_p} \left( \frac{nR}{Q + pV} \right) \quad (\text{A1-5})$$

we obtain:

$$\int_{B_0}^{B_1} \left[ \ln \left( \frac{B}{G} \right) \right]^2 \frac{dB}{B} = -HD \quad (\text{A1-6})$$

where  $B_0$  is the value of  $B$  at time zero and  $B_1$  is the value at time  $t$  and the variable  $D$  (Eq. (8)) represents the total work done locally by deformation of the medium. Evaluating the integral:

$$\frac{(\ln B_1 - \ln B_0)}{\ln(B_0/G) \ln(B_1/G)} = -HD \quad (\text{A1-7})$$

and using Eqs. (A1-5) and (A1-3) we then obtain Eq. (10):

$$\ln \left( \frac{B_1}{B_0} \right) = -\sqrt{(T_1 T_0)} D \quad (\text{A1-8})$$

## Appendix 2

A consistent treatment of the thermal energy balance (with typical simplifying assumptions) for a thermal anomaly which varies rapidly in a horizontal direction (perpendicular to the hypothetical shear zone), and is relatively constant in the other two directions follows from the relevant diffusion equation:

$$\rho C_p \frac{\partial T}{\partial t} = -\lambda \frac{\partial^2 T}{\partial x^2} + \Phi \quad (\text{A2-1})$$

where  $\Phi$  is the rate of shear heating and  $\lambda$  is thermal conductivity. When diffusion is assumed negligible ( $\lambda = 0$ ) we use

$$\rho C_p \frac{\partial T}{\partial t} = \Phi = \dot{\epsilon}_{ij} \tau_{ij} \quad (\text{A2-2})$$

and the thermal anomaly  $\Delta T$  relative to an original background temperature (assumed constant) is simply proportional to the work done by viscous deformation:

$$\Delta T = \frac{D}{\rho C_p} \quad (\text{A2-3})$$

where  $D$  is defined by Eq. (8). This temperature anomaly must also satisfy (Eq. (A2-1)) above, so the effect of thermal diffusion can be represented in this model by treating  $D$  as a proxy for the local temperature anomaly:

$$\frac{\partial D}{\partial t} = -\kappa \frac{\partial^2 D}{\partial x^2} + \Phi \quad (\text{A2-4})$$

where the thermal diffusivity,  $\kappa$ , is related to thermal diffusion ( $\lambda$ ) by:

$$\kappa = \frac{\lambda}{\rho C_p} \quad (\text{A2-5})$$

If  $D$  has a harmonic variation with a characteristic wavenumber  $k$  in the  $x$  direction, then:

$$\frac{\partial D}{\partial t} = -\kappa k^2 D + \Phi \quad (\text{A2-6})$$

and hence we obtain Eq. (13) with  $\beta$  defined by Eq. (14).

## References

- Allam, A.A., Ben-Zion, Y., 2012. Seismic velocity structures in the southern California plate-boundary environment from double-difference tomography. *Geophys. J. Int.* 190 (2), 1181–1196. <https://doi.org/10.1111/j.1365-246X.2012.05544.x>.
- Altuncu-Poyraz, S., Teoman, M.U., Türkelli, N., Kahraman, M., Cambaz, D., Mutlu, A., Rost, S., Houseman, G.A., Thompson, D.A., Cornwell, D., Utkucu, M., Gülen, L., 2015. New constraints on micro-seismicity and stress state in the western part of the North Anatolian Fault Zone: observations from a dense seismic array. *Tectonophysics* 656, 190–201. <https://doi.org/10.1016/j.tecto.2015.06.022>.
- Baris, S., Nakajima, J., Hasegawa, A., Honkura, Y., Ito, A., Ucer, B., 2005. Three-dimensional structure of  $V_p$ ,  $V_s$  and  $V_p/V_s$  in the upper crust of the Marmara region, NW Turkey. *Earth Planets Space* 57 (11), 1019–1038. <https://doi.org/10.1186/BF03351882>.
- Beaumont, C., Muñoz, J.A., Hamilton, J., Fullsack, P., 2000. Factors controlling the Alpine evolution of the central Pyrenees inferred from a comparison of observations and geodynamical models. *J. Geophys. Res. Solid Earth* 105 (B4), 8121–8145. <https://doi.org/10.1029/1999JB900390>.
- Bradbury, K.K., Evans, J.P., Chester, J.S., Chester, F.M., Kirschner, D.L., 2011. Lithology and internal structure of the San Andreas fault at depth based on characterization of phase 3 whole-rock core in the San Andreas Fault Observatory at Depth (SAFOD) borehole. *Earth Planet. Sci. Lett.* 310 (1), 131–144. <https://doi.org/10.1016/j.epsl.2011.07.020>.
- Brun, J.-P., 2002. Deformation of the continental lithosphere: Insights from brittle-ductile models. In: DeMeer, S., Rury, M.R., DeBresser, J.H.P., Pennock, G.M. (Eds.), *Deformation Mechanisms, Rheology and Tectonics: Current Status and Future Perspectives*. The Geological Society.
- Brun, J., Cobbold, P., 1980. Strain heating and thermal softening in continental shear zones: a review. *Journal of Structural Geology* 2 (1), 149–158. [https://doi.org/10.1016/0191-8141\(80\)90045-0](https://doi.org/10.1016/0191-8141(80)90045-0).
- Burg, J.-P., Schmalholz, S., 2008. Viscous heating allows thrusting to overcome crustal-scale buckling: numerical investigation with application to the Himalayan syntaxes. *Earth Planet. Sci. Lett.* 274 (1–2), 189–203. <https://doi.org/10.1016/j.epsl.2008.07.022>.
- Burgmann, R., Dresen, G., 2008. Rheology of the lower crust and upper mantle: evidence from rock mechanics, geodesy, and field observations. *Annu. Rev. Earth Planet. Sci.* 36, 531–567. <https://doi.org/10.1146/annurev.earth.36.031207.124326>.

- Calignano, E., Sokoutis, D., Willingshofer, E., Gueydan, F., Cloetingh, S., 2015. Strain localization at the margins of strong lithospheric domains: insights from analogue models. *Tectonics* 34 (3), 396–412. <https://doi.org/10.1002/2014TC003756>.
- Cerca, M., Ferrari, L., Bonini, M., Corti, G., Manetti, P., 2004. The role of crustal heterogeneity in controlling vertical coupling during Laramide shortening and the development of the Caribbean-North America transform boundary in southern Mexico: insights from analogue models. *Geol. Soc. Spec. Publ.* 227 (1), 117–139. <https://doi.org/10.1144/GSL.SP.2004.227.01.07>.
- Chen, P., Zhao, L., Jordan, T.H., 2007. Full 3D tomography for the crustal structure of the Los Angeles Region. *BSSA* 97 (4), 1094. <https://doi.org/10.1785/0120060222>.
- Cloetingh, S., van Wees, J., Ziegler, P., Lenkey, L., Beekman, F., Tesauro, M., Förster, A., Norden, B., Kaban, M., Hardebol, N., Bonté, D., Genter, A., Guillou-Frottier, L., Voorde, M.T., Sokoutis, D., Willingshofer, E., Cornu, T., Worum, G., 2010. Lithospheric tectonics and thermo-mechanical properties: an integrated modelling approach for enhanced geothermal systems exploration in Europe. *Earth Sci. Rev.* 102 (3–4), 159–206. <https://doi.org/10.1016/j.earscirev.2010.05.003>.
- Corti, G., Bonini, M., Mazzarini, F., Boccaletti, M., Innocenti, F., Manetti, P., Mulugeta, G., Sokoutis, D., 2002. Magma-induced strain localization in centrifuge models of transfer zones. *Tectonophysics* 348 (4), 205–218. [https://doi.org/10.1016/S0040-1951\(02\)00063-X](https://doi.org/10.1016/S0040-1951(02)00063-X).
- Cowie, P.A., Scholz, C.H., 1992. Physical explanation for the displacement-length relationship of faults using a post-yield fracture mechanics model. *J. Struct. Geol.* 14 (10), 1133–1148. [https://doi.org/10.1016/0191-8141\(92\)90065-5](https://doi.org/10.1016/0191-8141(92)90065-5).
- Dayem K. E., Houseman G. A. and Molnar P. (2009) Localization of shear along a lithospheric strength discontinuity: application of a continuous deformation model to the boundary between Tibet and the Tarim Basin. *Tectonics* 28, TC3002. doi:<https://doi.org/10.1029/2008TC002264>
- England, P., Houseman, G., 1985. Role of lithospheric strength heterogeneities in the tectonics of Tibet and neighbouring regions. *Nature* 315, 297–301. <https://doi.org/10.1038/315297a0>.
- England, P., Molnar, P., 2005. Late Quaternary to decadal velocity fields in Asia. *J. Geophys. Res. Solid Earth* 110 (B12). <https://doi.org/10.1029/2004JB003541>.
- England, P., Houseman, G., Nocquet, J.-M., 2016. Constraints from GPS measurements on the dynamics of deformation in Anatolia and the Aegean. *J. Geophys. Res. Solid Earth* 121 (12), 8888–8916. <https://doi.org/10.1002/2016JB013382>.
- Ford, H.A., Fischer, K.M., Lekic, V., 2014. Localized shear in the deep lithosphere beneath the San Andreas fault system. *Geology* 42 (4), 295. <https://doi.org/10.1130/G35128.1>.
- Grujic, D., Mancktelow, N.S., 1998. Melt-bearing shear zones: analogue experiments and comparison with examples from southern Madagascar. *J. Struct. Geol.* 20 (6), 673–680. [https://doi.org/10.1016/S0191-8141\(98\)00006-6](https://doi.org/10.1016/S0191-8141(98)00006-6).
- Gueydan, F., Précigout, J., Montési, L.G., 2014. Strain weakening enables continental plate tectonics. *Tectonophysics* 631, 189–196. <https://doi.org/10.1016/j.tecto.2014.02.005>.
- Hirth, G., Kohlstedt, D.L., 1995. Experimental constraints on the dynamics of the partially molten upper mantle: 2. Deformation in the dislocation creep regime. *J. Geophys. Res.* 100 (B8), 15441–15449. <https://doi.org/10.1029/95JB01292>.
- Hirth, G. & Kohlstedt, D. (2013). Rheology of the Upper Mantle and the Mantle Wedge: A View from the Experimentalists. In: Eiler, J. (Ed.), *Inside the Subduction Factory*, American Geophysical Union. doi:<https://doi.org/10.1029/138GM06>
- Hirth, G., Teysier, C., Dunlap, W.J., 2001. An evaluation of quartzite flow laws based on comparisons between experimentally and naturally deformed rocks. *Int. J. Earth Sci.* 90 (1), 77–87. <https://doi.org/10.1007/s005310000152>.
- Holdsworth, R., van Diggelen, E., Spiers, C., de Bresser, J., Walker, R., Bowen, L., 2011. Fault rocks from the SAFOD core samples: implications for weakening at shallow depths along the San Andreas Fault, California. *J. Struct. Geol.* 33 (2), 132–144. <https://doi.org/10.1016/j.jsg.2010.11.010>.
- Hussain, E., Wright, T.J., Walters, R.J., Bekaert, D.P.S., Lloyd, R., Hooper, A., 2018. Constant strain accumulation rate between major earthquakes on the North Anatolian Fault. *Nat. Commun.* 9 (1), 1392. <https://doi.org/10.1038/s41467-018-03739-2>.
- Kahraman, M., Cornwell, D.G., Thompson, D.A., Rost, S., Houseman, G.A., Türkelli, N., Teoman, U., Poyraz, S.A., Utkucu, M., Gülen, L., 2015. Crustal-scale shear zones and heterogeneous structure beneath the North Anatolian Fault Zone, Turkey, revealed by a high-density seismometer array. *Earth Planet. Sci. Lett.* 430, 129–139. <https://doi.org/10.1016/j.epsl.2015.08.014>.
- Karato, S.-I., 1984. Grain-size distribution and rheology of the upper mantle. *Tectonophysics* 104 (1), 155–176. [https://doi.org/10.1016/0040-1951\(84\)90108-2](https://doi.org/10.1016/0040-1951(84)90108-2).
- Karato, S.-I., Wu, P., 1993. Rheology of the upper mantle: a synthesis. *Science* 260 (5109), 771–778. <https://doi.org/10.1126/science.260.5109.771>.
- Karato, S.-I., Paterson, M.S., FitzGerald, J.D., 1986. Rheology of synthetic olivine aggregates: influence of grain size and water. *J. Geophys. Res. Solid Earth* 91 (B8), 8151–8176. <https://doi.org/10.1029/JB091iB08p08151>.
- Kaus, B.J.P., Podladchikov, Y.Y., 2006. Initiation of localized shear zones in viscoelastic-plastic rocks. *J. Geophys. Res.* 111 (B4). <https://doi.org/10.1029/2005JB003652>.
- Keep, M., 2000. Models of lithospheric-scale deformation during plate collision: effects of indenter shape and lithospheric thickness. *Tectonophysics* 326 (3–4), 203–216. [https://doi.org/10.1016/S0040-1951\(00\)00123-2](https://doi.org/10.1016/S0040-1951(00)00123-2).
- Kohlstedt, D.L., Goetze, C., 1974. Low-stress high-temperature creep in olivine single crystals. *J. Geophys. Res.* 79 (14), 2045–2051. <https://doi.org/10.1029/JB079i014p02045>.
- Kreemer, C., Blewitt, G., Klein, E.C., 2014. A geodetic plate motion and global strain rate model. *Geochem. Geophys. Geosyst.* 15, 3849–3889. <https://doi.org/10.1002/2014GC005407>.
- Le Pourhiet L., Huet B., May D. A., Labrousse L. and Jolivet L. (2012) Kinematic interpretation of the 3D shapes of metamorphic core complexes. *Geochem. Geophys. Geosyst.* 13 (9), Q09002. doi:<https://doi.org/10.1029/2012GC004271>
- Leloup, P.H., Ricard, Y., Battaglia, J., Lacassin, R., 1999. Shear heating in continental strike-slip shear zones: model and field examples. *Geophys. J. Int.* 136, 19–40. <https://doi.org/10.1046/j.1365-246X.1999.00683.x>.
- Lin, G., Shearer, P.M., Hauksson, E., 2007. Applying a three-dimensional velocity model, waveform cross correlation, and cluster analysis to locate southern California seismicity from 1981 to 2005. *J. Geophys. Res. Solid Earth* 112 (B12309). <https://doi.org/10.1029/2007JB004986>.
- Mandal, N., Misra, S., Samanta, S.K., 2004. Role of weak flaws in nucleation of shear zones: an experimental and theoretical study. *J. Struct. Geol.* 26 (8), 1391–1400. <https://doi.org/10.1016/j.jsg.2004.01.001>.
- McClusky, S., Balassanian, S., Barka, A., Demir, C., Ergintav, S., Georgiev, I., Gurkan, O., Hamburger, M., Hurst, K., Kahle, H., Kastens, K., Kekelidze, G., King, R., Kotzev, V., Lenk, O., Mahmoud, S., Mishin, A., Nadariya, M., Ouzounis, A., Paradissis, D., Peter, Y., Prilepin, M., Reilinger, R., Sanli, I., Seeger, H., Tealeb, A., Toksöz, M.N., Veis, G., 2000. Global positioning system constraints on plate kinematics and dynamics in the eastern Mediterranean and Caucasus. *J. Geophys. Res. Solid Earth* 105 (B3), 5695–5719. <https://doi.org/10.1029/1999JB900351>.
- Misra, S., Mandal, N., 2007. Localization of plastic zones in rocks around rigid inclusions: insights from experimental and theoretical models. *J. Geophys. Res. Solid Earth* 112 (B9), B09206. <https://doi.org/10.1029/2006JB004328>.
- Misra, S., Mandal, N., Dasgupta, S., 2015. Role of pressure and temperature in inclusion-induced shear localization: an analogue experimental approach. *J. Struct. Geol.* 81, 78–88. <https://doi.org/10.1016/j.jsg.2015.10.004>.
- Molnar, P., Tapponnier, P., 1981. A possible dependence of tectonic strength on the age of the crust in Asia. *Earth Planet. Sci. Lett.* 52 (1), 107–114. [https://doi.org/10.1016/0012-821X\(81\)90213-2](https://doi.org/10.1016/0012-821X(81)90213-2).
- Montési, L.G.J., 2013. Fabric development as the key for forming ductile shear zones and enabling plate tectonics. *J. Struct. Geol.* 50, 254–266. <https://doi.org/10.1016/j.jsg.2012.12.011>.
- Montési, L.G.J., Zuber, M.T., 2002. A unified description of localization for application to large-scale tectonics. *J. Geophys. Res. Solid Earth* 107 (B3), 1–21. <https://doi.org/10.1029/2001JB000465>.
- Moore, M.A., 1999. *Crustal deformation in the southern New Zealand region*. D.Phil. University of Oxford.
- Moore, J.D., Parsons, B., 2015. Scaling of viscous shear zones with depth-dependent viscosity and power-law stress-strain-rate dependence. *Geophys. J. Int.* 202 (1), 242–260. <https://doi.org/10.1093/gji/ggv143>.
- Munteanu, I., Willingshofer, E., Sokoutis, D., Matenco, L., Dinu, C., Cloetingh, S., 2013. Transfer of deformation in back-arc basins with a laterally variable rheology: constraints from analogue modelling of the Balkanides–Western Black Sea inversion. *Tectonophysics* 602, 223–236. <https://doi.org/10.1016/j.tecto.2013.03.009>.
- Nazareth, J.J., Hauksson, E., 2004. The seismogenic thickness of the Southern California crust. *BSSA* 94 (3), 940. <https://doi.org/10.1785/0120020129>.
- Nicolas A., Bouchez J., Blaise J. and Poirier J. (1977) Geological aspects of deformation in continental shear zones. *Tectonophysics* 42 (1), 55-73. doi:10.1016/0040-1951(77)90017-8
- Ozakin, Y., Ben-Zion, Y., 2015. Systematic receiver function analysis of the Moho geometry in the Southern California plate-boundary region. *Pure Appl. Geophys.* 172 (5), 1167–1184. <https://doi.org/10.1007/s00024-014-0924-6>.
- Papaleo, E., Cornwell, D.G., Rawlinson, N., 2017. Seismic tomography of the North Anatolian Fault: new insights into structural heterogeneity along a continental strike-slip fault. *Geophys. Res. Lett.* 44 (5), 2186–2193. <https://doi.org/10.1002/2017GL072726>.
- Pfister, M., Rybach, L., Simsek, S., 1998. Geothermal reconnaissance of the Marmara Sea region (NW Turkey): surface heat flow density in an area of active continental extension. *Tectonophysics* 291 (1), 77–89. [https://doi.org/10.1016/S0040-1951\(98\)00032-8](https://doi.org/10.1016/S0040-1951(98)00032-8).
- Pitzer, K.S., Sterner, S.M., 1994. Equations of state valid continuously from zero to extreme pressures with H<sub>2</sub>O and CO<sub>2</sub> as examples. *Int. J. Thermophys.* 16 (2), 511–518. <https://doi.org/10.1007/BF01441917>.
- Précigout, J., Gueydan, F., 2009. Mantle weakening and strain localization: implications for the long-term strength of the continental lithosphere. *Geology* 37 (2), 147–150. <https://doi.org/10.1130/G25239A.1>.
- Précigout, J., Gueydan, F., Gapais, D., Garrido, C.J., Essaifi, A., 2007. Strain localisation in the subcontinental mantle — a ductile alternative to the brittle mantle. *Tectonophysics* 445, 318–336. <https://doi.org/10.1016/j.tecto.2007.09.002>.
- Prescott, W.H., Savage, J.C., Svarc, J.L., Manaker, D., 2001. Deformation across the Pacific-North America plate boundary near San Francisco, California. *J. Geophys. Res.* 106 (B4), 6673–6682. <https://doi.org/10.1029/2000JB900397>.
- Regenauer-Lieb, K., Rosenbaum, G., Lyakhovskiy, V., Liu, J., Weinberg, R., Segev, A., Weinstein, Y., 2015. Melt instabilities in an intraplate lithosphere and implications for volcanism in the Harrat Ash-Shaam volcanic field (NW Arabia). *J. Geophys. Res. Solid Earth* 120 (3), 1543–1558. <https://doi.org/10.1002/2014JB011403>.
- Rutter, E.H., Brodie, K.H., 2004. Experimental grain size-sensitive flow of hot-pressed Brazilian quartz aggregates. *J. Struct. Geol.* 26 (11), 2011–2023. <https://doi.org/10.1016/j.jsg.2004.04.006>.
- Rybacki, E., Dresen, G., 2000. Dislocation and diffusion creep of synthetic anorthite aggregates. *J. Geophys. Res.* 105 (B11), 26017–26036. <https://doi.org/10.1029/2000JB900223>.
- Salah, M.K., Sahin, S., Kaplan, M., 2007. Seismic velocity structure along the western segment of the North Anatolian Fault Zone imaged by seismic tomography. *Bull. Earthquake Res. Inst.* 82, 209–223.
- Sass, J.H., Williams, C.F., Lachenbruch, A.H., Galanis, S.P., Grubb, F.V., 1997. Thermal regime of the San Andreas Fault near Parkfield. California. *J. Geophys. Res. Solid Earth* 102 (B12), 27575–27585. <https://doi.org/10.1029/JB102iB12p27575>.
- Savage, J.C., Burford, R.O., 1973. Geodetic determination of relative plate motion in

- Central California. *J. Geophys. Res.* 78 (5), 832–845.
- Segall, P., 2002. Integrating geologic and geodetic estimates of slip rate on the San Andreas Fault System. *Int. Geol. Rev.* 44 (1), 62–82. <https://doi.org/10.2747/0020-6814.44.1.62>.
- Sengor, A.M.C., Tuysuz, O., Imren, C., Sakinc, M., Eyidogan, H., Gorgou, N., Rangin, C., Pichon, X.L., 2005. The North Anatolian fault: a new look. *Annu. Rev. Earth Planet. Sci.* 33, 37–112. <https://doi.org/10.1146/annurev.earth.32.101802.120415>.
- Shen, Z.-K., Jackson, D.D., Ge, B.X., 1996. Crustal deformation across and beyond the Los Angeles basin from geodetic measurements. *J. Geophys. Res.* 101 (B12), 27957–27980. <https://doi.org/10.1029/96JB02544>.
- Smith-Konter, B.R., Sandwell, D.T., Shearer, P., 2011. Locking depths estimated from geodesy and seismology along the San Andreas Fault System: implications for seismic moment release. *J. Geophys. Res. Solid Earth* 116 (B06401). <https://doi.org/10.1029/2010JB008117>.
- Sokoutis, D., Burg, J.-P., Bonini, M., Corti, G., Cloetingh, S., 2005. Lithospheric-scale structures from the perspective of analogue continental collision. *Tectonophysics* 406, 1–2), 1–15. <https://doi.org/10.1016/j.tecto.2005.05.025>.
- Sternner, S.M., Pitzer, K.S., 1994. An equation of state for carbon dioxide valid from zero to extreme pressures. *Contrib. Mineral. Petrol* 117 (4), 362–374. <https://doi.org/10.1007/BF00307271>.
- Taylor, G., Rost, S., Houseman, G., 2016. Crustal imaging across the North Anatolian Fault Zone from the autocorrelation of ambient seismic noise. *Geophys. Res. Lett.* 43 (6), 2502–2509. <https://doi.org/10.1002/2016GL067715>.
- Thatcher, W., England, P.C., 1998. Ductile shear zones beneath strike-slip faults: implications for the thermomechanics of the San Andreas Fault Zone. *J. Geophys. Res.* 103 (B1), 891–905. <https://doi.org/10.1029/97JB02274>.
- Thielmann, M., Kaus, B.J., 2012. Shear heating induced lithospheric-scale localization: does it result in subduction? *Earth Planet. Sci. Lett.* 359–360, 1–13. <https://doi.org/10.1016/j.epsl.2012.10.002>.
- Thurber, C., Roecker, S., Zhang, H., Baher, S., Ellsworth, W., 2004. Fine scale structure of the San Andreas fault zone and location of the SAFOD target earthquakes. *Geophys. Res. Lett.* 31 (12). <https://doi.org/10.1029/2003GL019398>.
- Thurber, C., Zhang, H., Waldhauser, F., Hardebeck, J., Michael, A., Eberhart-Phillips, D., 2006. Three-dimensional compressional wavespeed model, earthquake relocations, and focal mechanisms for the Parkfield, California, Region. *BSSA* 96 (4B), S38. <https://doi.org/10.1785/0120050825>.
- Titus, S.J., Dyson, M., DeMets, C., Tikoff, B., Rolandone, F., Bürgmann, R., 2011. Geologic versus geodetic deformation adjacent to the San Andreas Fault, central California. *Geol. Soc. Am. Bull.* 123 (5–6), 794. <https://doi.org/10.1130/B30150.1>.
- Tommasi, A., Vauchez, A., 1997. Continental-scale rheological heterogeneities and complex intraplate tectono-metamorphic patterns: insights from a case-study and numerical models. *Tectonophysics* 279 (1), 327–350. [https://doi.org/10.1016/S0040-1951\(97\)00117-0](https://doi.org/10.1016/S0040-1951(97)00117-0).
- Tommasi, A., Vauchez, A., Daudré, B., 1995. Initiation and propagation of shear zones in a heterogeneous continental lithosphere. *J. Geophys. Res. Solid Earth* 100 (B11), 22083–22101. <https://doi.org/10.1029/95JB02042>.
- Vauchez, A., Tommasi, A., Barruol, G., 1998. Rheological heterogeneity, mechanical anisotropy and deformation of the continental lithosphere. *Tectonophysics* 296 (1–2), 61–86. [https://doi.org/10.1016/S0040-1951\(98\)00137-1](https://doi.org/10.1016/S0040-1951(98)00137-1).
- Vauchez, A., Tommasi, A., Mainprice, D., 2012. Faults (shear zones) in the Earth's mantle. *Tectonophysics* 558–559, 1–27. <https://doi.org/10.1016/j.tecto.2012.06.006>.
- Warren, J.M., Hirth, G., 2006. Grain size sensitive deformation mechanisms in naturally deformed peridotites. *Earth Planet. Sci. Lett.* 248 (1), 438–450. <https://doi.org/10.1016/j.epsl.2006.06.006>.
- Willingshofer, E., Sokoutis, D., Burg, J.-P., 2005. Lithospheric-scale analogue modelling of collision zones with a pre-existing weak zone. *Geol. Soc. Spec. Publ.* 243, 277–294. <https://doi.org/10.1144/GSL.SP.2005.243.01.18>.
- Wright, T.J., Elliott, J.R., Wang, H., Ryder, I., 2013. Earthquake cycle deformation and the Moho: implications for the rheology of continental lithosphere. *Tectonophysics* 609, 504–523. <https://doi.org/10.1016/j.tecto.2013.07.029>.
- Yamasaki, T., Wright, T.J., Houseman, G.A., 2014. Weak ductile shear zone beneath a major strike-slip fault: Inferences from earthquake cycle model constrained by geodetic observations of the western North Anatolian Fault Zone. *J. Geophys. Res. Solid Earth* 119, 3678–3699. <https://doi.org/10.1002/2013JB010347>.
- Yan, Z., Clayton, R.W., 2007. Regional mapping of the crustal structure in southern California from receiver functions. *J. Geophys. Res. Solid Earth* 112 (B05311). <https://doi.org/10.1029/2006JB004622>.
- Yardley, B.W.D., Bodnar, R.J., 2014. Fluids in the continental crust. *Geochem. Perspect.* 3 (1), 1–127. <https://doi.org/10.7185/geochempersp.3.1>.
- Yolsal-Çevikbilen, S., Biryol, C.B., Beck, S., Zandt, G., Taymaz, T., Adiyaman, H.E., Özacar, A.A., 2012. 3-D crustal structure along the North Anatolian Fault Zone in north-central Anatolia revealed by local earthquake tomography. *Geophys. J. Int.* 188 (3), 819–849. <https://doi.org/10.1111/j.1365-doi:10.1111/j.1365-246X.2011.05313.x>.
- Yuen, D.A., Fleitout, L., Schubert, G., Froidevaux, C., 1978. Shear deformation zones along major transform faults and subducting slabs. *Geophys. J. R. Astron. Soc.* 54 (1), 93–119. <https://doi.org/10.1111/j.1365-246X.1978.tb06758.x>.
- Zhu, L., 2000. Crustal structure across the San Andreas Fault, southern California from teleseismic converted waves. *Earth Planet. Sci. Lett.* 179 (1), 183–190. [https://doi.org/10.1016/S0012-821X\(00\)00101-1](https://doi.org/10.1016/S0012-821X(00)00101-1).